ACS OMEGA

Open Access

http://pubs.acs.org/journal/acsodf

Article

Comparative Study of TiO_2, ZnO, and Nb_2O_5 Photoanodes for Nitro-Substituted Naphthoquinone Photosensitizer-Based Solar Cells

Niyamat I. Beedri, Gaurav Dani, Manisha Gaikwad, Habib M. Pathan, and Sunita Salunke-Gawali*

Cite This: *ACS Omega* 2023, 8, 38748−38765

Read Online

ACCESS | Metrics & More | Article Recommendations

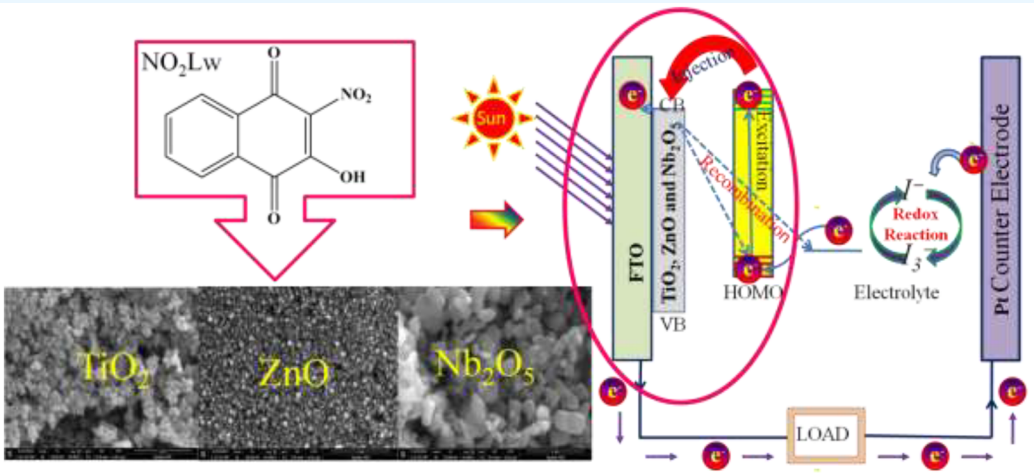

ABSTRACT: This research focuses on the first demonstration of NO_2Lw (2-hydroxy-3-nitronaphthalene-1,4-dione) as a photosensitizer and TiO_2, ZnO, and Nb_2O_5 as photoanode materials for dye-sensitized solar cells (DSSCs). The metal-free organic photosensitizer (i.e., nitro-group-substituted naphthoquinone, NO_2Lw) was synthesized for this purpose. As a photoanode material, metal oxides, such as TiO_2, ZnO, and Nb_2O_5, were selected. The synthesized NO_2Lw contains an electron-withdrawing group ($-NO_2$) and anchoring groups ($-OH$) that exhibit absorption in the visible range. The UV−visible absorbance spectrum of NO_2Lw demonstrates the absorption ascribed to ultraviolet and visible region charge transfer. The NO_2Lw interacts with the TiO_2, ZnO, and Nb_2O_5 photoanode, as shown by bathochromic shifts in wavelengths in the photosensitizer-loaded TiO_2, ZnO, and Nb_2O_5 photoanodes. FT-IR analysis also studied the bonding interaction between NO_2Lw and TiO_2, ZnO, and Nb_2O_5 photoanode material. The TiO_2, ZnO, and Nb_2O_5 photoanodes loaded with NO_2Lw exhibit a shift in the wavenumber of the functional groups, indicating that these groups were involved in loading the NO_2Lw photosensitizer. The amount of photosensitizer loading was calculated, showing that TiO_2 has higher loading than ZnO and Nb_2O_5 photoanodes; this factor may constitute an increased J_{SC} value of the TiO_2 photoanode. The device performance is compared using photocurrent−voltage (J−V) curves; electrochemical impedance spectroscopy (EIS) measurement examines the device's charge transport. The TiO_2 photoanode showed higher performance than the ZnO and Nb_2O_5 photoanodes in terms of photoelectrochemical properties. When compared to ZnO and Nb_2O_5 photoanodes-based DSSCs, the TiO_2 photoanode Bode plot shows a signature frequency peak corresponding to electron recombination rate toward the low-frequency region, showing that TiO_2 has a greater electron lifetime than ZnO and Nb_2O_5 photoanodes based DSSCs.

1. INTRODUCTION

Energy becomes sustainable when it is harvested from naturally occurring sources without having a negative impact on the environment.[1] Sustainable energy includes all renewable energy sources like geothermal, biomass, wind, tidal, and solar, apart from others.[2] It helps in maintaining the natural environment by using eco-friendly materials to serve the ever-increasing needs of the growing world population.[3] It is a viable energy source compared to the traditional sources,

Received: August 23, 2023
Accepted: September 15, 2023
Published: October 2, 2023

Table 1. DSSCs Performance of Different Semiconducting Oxides as Photoanode Material with Several Synthesized Derivatives of Quinone-based Photosensitizer from the Literature along with NO_2Lw Photosensitizer

Photoanode Material	Photosensitizer	λ_{max} (nm)	E_{0-0} (eV)	V_{oc} (V)	J_{sc} (mA/cm^2)	FF	PCE (%)	Ref.
TiO_2	2-chloro-3[(pyridine-2-ylmethyl)amino]naphthalene-1,4-dione (2AMP)	458	2.42	0.54	0.69	61	0.22	59
TiO_2	2-chloro-3[(pyridine-3-ylmethyl)amino]naphthalene-1,4-dione (3AMP)	460	2.33	0.51	0.65	83	0.27	59
TiO_2	2-chloro-3[(2-pyridine-2-ylethyl)amino)]naphthalene-1,4-dione (2AEP)	466	2.37	0.50	0.53	54	0.14	59
ZnO	2-chloro-3[(pyridine-2-ylmethyl)amino]naphthalene-1,4-dione (2AMP)	458	2.42	0.53	0.68	60	0.22	59
ZnO	2-chloro-3[(pyridine-3-ylmethyl)amino]naphthalene-1,4-dione (3AMP)	460	2.33	0.52	0.64	69	0.23	59
ZnO	2-chloro-3[(2-pyridine-2-ylethyl)amino)]naphthalene-1,4-dione (2AEP)	466	2.37	0.30	0.57	66	0.11	59
TiO_2	2-hydroxy-3-[phenyl(phenylamino)methyl] naphthalene-1,4-dione (4a)	411	2.68	0.29	0.035	50	–	57
ZnO	4-(3-chloro-1,4-dioxo-1,4-dihydronaphthalen-2-ylamino) benzoic acid	482	2.75	0.392	3.196	60	0.75	60
TiO_2	2-hydroxy-3-[(4-methoxyphenyl](p-tolylamino)methyl] naphthalene-1,4-dione (4-OMe)	456	2.20	0.36	0.053	57	0.01	58
TiO_2	2-hydroxy-3-[p-toly (p-tolylamino)methyl] naphthalene-1,4-dione (4-Me)	444	2.20	0.37	0.045	56	0.009	58
TiO_2	2-[(4-Bromophenyl) (p-tolylamino)methy]-3-hydroxy naphthalene-1,4-dione (4-Br)	454	2.30	0.34	0.034	58	0.007	58
TiO_2	2-[(2-Chlorophenyl) (p-tolylamino)methy]-3-hydroxy naphthalene-1,4-dione (2-Cl)	433	2.30	0.31	0.026	54	0.004	58
TiO_2	2-[(2,4-Dichlorophenyl) (p-tolylamino)methy]-3-hydroxy naphthalene-1,4-dione (2,4-diCl)	455	2.30	0.26	0.022	46	0.003	58
TiO_2 NR (300 °C)	2-bromo-3-(methylamino)naphthalene-1,4-dione (BrA1)	471	2.33	0.50	0.48	44	0.10	61
TiO_2 NR (400 °C)	2-bromo-3-(methylamino)naphthalene-1,4-dione (BrA1)	471	2.33	0.55	0.60	48	0.16	61
TiO_2 NR (500 °C)	2-bromo-3-(methylamino)naphthalene-1,4-dione (BrA1)	471	2.33	0.52	0.63	46	0.15	61
TiO_2 NR (600 °C)	2-bromo-3-(methylamino)naphthalene-1,4-dione (BrA1)	471	2.33	0.51	0.55	40	0.11	61
ZrO_2	6-methyl-5H-benzo[α]phenothiazin-5-one	477	1.88	0.42	3.01	20	1.64	62
ZnO	2-hydroxy-1,4-naphthoquinone	462	–	0.52	1.80	62	0.56	63
TiO_2	2-hydroxy-1,4-naphthoquinone	410	2.70	0.54	0.92	50	0.31	64
TiO_2	3-hydroxy-4-(hydroxyimino) naphthalen -1 (4H)-one (LwOx)	407	2.85	0.41	0.28	37	0.04	65
TiO_2	3-hydroxy-4-(hydroxyimino)-2- methylnaphthalen -1(4H)-one (PthOx)	413	2.71	0.28	0.15	32	0.01	65
TiO_2	2-chloro-3-hydroxy-4-(hydroxyimino) naphthalen-1(4H)-one (Cl_LwOx)	402	2.87	0.47	0.78	38	0.14	65
ZnO	2-propylamine-1,4-naphthoquinone (HA3)	452	–	0.29	1.21	35	0.12	66
ZnO	2-butylamino-1,4-naphthoquinone (HA4)	452	–	0.32	0.71	38	0.09	66
ZnO	2-bromo-3-propylamino-1,4-naphthoquinone (BrA3)	471	–	0.33	1.01	39	0.13	66
ZnO	2-bromo-3-butylamino-1,4-naphthoquinone (BrA4)	471	–	0.31	1.66	38	0.20	66
TiO_2	10-Chloro-6-methyl-5H benzo[α]phenoxazin-5-one (BPO_Cl)	451	2.49	0.56	0.430	–	–	67
TiO_2	6-methyl-5H-benzo[α]phenoxazin-5-one (BPO)	440	2.52	0.53	0.440	–	–	67
TiO_2	6-methyl-5H-benzo[α]phenothiazin-5-one (BPT)	474	2.33	0.49	0.240	–	–	67
ZnO	2-((thiophen-2-yl)methylamino)-3-chloro-naphthalene-1,4-dione (AMT)	464	–	0.21	0.17	60	0.02	68
ZnO	2-((thiophen-2-yl)ethylamino)-3-chloro-naphthalene-1,4-dione (AET)	469	–	0.22	0.22	59	0.03	68
TiO_2	2-((thiophen-2-yl)methylamino)-3-chloro-naphthalene-1,4-dione (AMT)	464	–	0.41	1.73	33	0.23	68
TiO_2	2-((thiophen-2-yl)ethylamino)-3-chloro-naphthalene-1,4-dione (AET)	469	–	0.42	1.73	44	0.32	68
TiO_2	2-hydroxy-1,4-naphthoquinone	–	–	0.66	2.21	63	0.93	69
P-type NiO	$KuQCH_3$	–	2.17	0.90	0.74	35	0.02	70
P-type NiO	$KuQ3CO_2H$	–	2.21	0.92	0.74	35	0.02	70
P-type NiO	$KuQ8CO_2H$	–	2.19	0.99	0.63	36	0.02	70
TiO_2	2-hydroxy-3-nitronaphthalene-1,4-dione (NO_2Lw)	391	2.87	0.44	0.82	40	0.14	present study
ZnO	2-hydroxy-3-nitronaphthalene-1,4-dione (NO_2Lw)	391	2.87	0.23	0.31	32	0.02	present study
Nb_2O_5	2-hydroxy-3-nitronaphthalene-1,4-dione (NO_2Lw)	391	2.87	0.24	0.16	42	0.01	present study

https://doi.org/10.1021/acsomega.3c06271
ACS Omega 2023, 8, 38748−38765

which are causing a tremendous load on Earth's ecosystem.[4] The entire world is already witnessing global warming and ever-increasing carbon emissions, leading to a pressing need of fulfilling global energy demand by using sustainable sources.[5]

Most daily activities require tremendous energy usage around the globe, leading to an excessive energy consumption. As the population and industrialization continue to grow, global energy consumption is rising quickly. One of this research's main aims is to meet the increasing global demand for energy consumption.[6,7] As a substitute for fossil fuels, nonfossil energy from clean sources is used. Examples of such sources include wind, water, biomass, geothermal, and solar energy because they are self-sufficient and less harmful to the ecosystem.[8−11] Solar energy is one of the most promising nonfossil options for tackling energy challenges with a less detrimental impact on the ecology.[12,13] Solar cells are an efficient device to convert solar energy into electrical energy[14,15] to meet the rising demand for energy around the globe.

Crystalline silicon performs reliably and efficiently and is considered the main compound in solar cell technology.[16] Still, it would be interesting to find cheaper alternatives due to the high cost of these complex technologies and expensive methods. Solar cells made of crystalline silicon are more costly and have a limited application.[17,18] Perovskite,[19,20] quantum-dot,[21] and dye[22]-sensitized solar cells are examples of third-generation solar cell technology that has met the requirement of a low-cost, straightforward fabrication process.[23−26] Over the past few years, dye-sensitized solar cells (DSSCs) have emerged as promising third-generation solar cell technology.[27,28] DSSCs make use of photovoltaic energy, making use of nontoxic and environment-friendly materials.[29] DSSCs have generated a lot of research attention because of their simple manufacturing process, low cost, ease of scaling up, nontoxicity, lighter weight,[30] and potential usage of the flexible substrate with transparent and colorful nature.[31]

The four main components used in the fabrication of DSSCs are the photoanode material (semiconductor), the dye molecule (a photosensitizer), the redox electrolyte, and the counter electrode.[32−37] In 1991, Grätzel and O'Regan published the first study on DSSCs using N3 dye as a photosensitizer.[38] Numerous studies in this field since the original work on DSSCs have primarily shown that various dyes (photosensitizers) have been molecularly engineered and used in DSSCs.[39−41] The production of novel photosensitizers that can be developed in DSSCs is an essential component affecting device efficiency.[42−44]

In the DSSCs, dyes based on ruthenium metals are primarily used as photosensitizers. In contrast, metal-free organic dyes have begun to take the position of ruthenium-metal-based dye.[45,46] Organic dyes are more affordable and environmentally friendly, with more significant molecular extinction coefficients and easily adjustable photophysical and electrochemical properties than their ruthenium-metal-based dye.[47,48] The compatibility of the photosensitizer is determined by understanding the molecular structures of these organic dyes and connecting them to their optical absorption spectral responses.[49] The photovoltaic performance of fabricated DSSCs can be reorganized following the photophysical, electrochemical, and structure−property relationships.[50] One essential molecular design requirement for DSSCs has been discovered as the donor-bridge-acceptor ($D-\pi-A$) system.[51] It showed improved solar spectrum light harvesting in visible regions.[52] Because it impacts the electrochemical and optical characteristics of the photosensitizer, intermolecular charge transfer (ICT) from donor to acceptor is essential for ensuring that DSSCs function correctly.[53] A photosensitizer's capacity for effective ICT from the HOMO localized donor moiety to the LUMO localized acceptor moiety correlates with enhanced light absorption and a lower HOMO−LUMO gap.[54]

Henna plant leaves are used to extract henna dyes. Henna leaves contain a derivative of naphthoquinone called 2-hydroxy-1,4-naphthoquinone (Lawsone). Using natural photosensitizers like Lawsone in DSSCs could be an eco-friendly and sustainable alternative to commercially available metal-based photosensitizers, often used to fabricate DSSCs. Semiconducting wide band gap materials such as TiO_2, ZnO, Nb_2O_5, CeO_2, and SnO_2 are employed as photoanode materials. These materials do not have an environmental impact during their manufacture and disposal process.[55] Metal-free organic photosensitizers such as coumarin and triphenylamine-, indoline-, and quinone-based photosensitizers are environmentally friendly compared to metal-containing photosensitizers.[56] Organic photosensitizers based on a naphthoquinone derivative has been used as an environmentally safe photosensitizer.[57] Naphthoquinone derivatives have an extensive range of molecular structures which could be used as photosensitizers.[58] Table 1 shows the DSSCs performance of different semiconducting oxides as photoanode materials with several synthesized derivatives of quinone-based photosensitizers from the literature along with NO_2Lw photosensitizer.

In the present investigation, a nitro-substituted naphthoquinone (NO_2Lw)-based photosensitizer was synthesized and has the molecular structure depicted in Figure 1a. NO_2Lw was synthesized with electron-withdrawing groups ($-NO_2$). On the moiety part, the impact of electron-withdrawing ($-NO_2$) substitutions is investigated concerning the photovoltaic performance of DSSCs. Specific appropriate peripheral

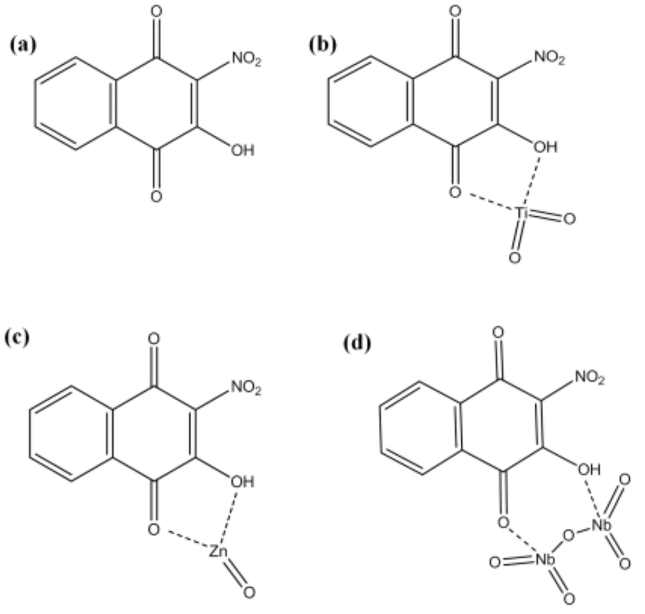

Figure 1. Molecular structure of photosensitizer (a) NO_2Lw (2-hydroxy-3-nitronaphthalene-1,4-dione) and schematic of the possible structure interfacial contact between (b) NO_2Lw and TiO_2, (c) NO_2Lw and ZnO, and (d) NO_2Lw and Nb_2O_5.

https://doi.org/10.1021/acsomega.3c06271
ACS Omega 2023, 8, 38748−38765

(−OH) functional groups for adsorption on the TiO_2, ZnO, and Nb_2O_5 surface are present in the photosensitizer.[71,72]

The lone pair of oxygens (hydroxyl group and carbonyl group) forms the bidentate complex by creating a five-member ring. Thus, the interface between the NO_2Lw and TiO_2, ZnO, and Nb_2O_5 is developed. The possible schematic interfacial contact structures of NO_2Lw and TiO_2, ZnO, and Nb_2O_5 are shown in Figures 1b, c, and d, respectively. The interaction of the hydroxyl group of NO_2Lw molecules with the valence-unfilled TiO_2, ZnO, and Nb_2O_5 surface facilitates the adsorption of the hydroxyl group of NO_2Lw molecules on the TiO_2, ZnO, and Nb_2O_5 surface. As a result of our investigation into naphthoquinone-based photosensitizers, the NO_2-substituted naphthoquinone-based photosensitizer has been reported by using the approach described in this article. This is the first demonstration of TiO_2, ZnO, and Nb_2O_5 as photoanodes and NO_2Lw as a photosensitizer for the DSSC application. Depending upon the energy levels of NO_2Lw, the conduction bands (CBs) of TiO_2, ZnO, and Nb_2O_5, and the amount of photosensitizer loading, we have successfully demonstrated the photovoltaic effect.

2. EXPERIMENTAL SECTION

2.1. Preparation of TiO_2, ZnO, and Nb_2O_5 Pastes. Using commercial TiO_2 (P25 Degussa, Nanoshel LLC, USA), ZnO, and Nb_2O_5 (Merck) nanopowders, TiO_2, ZnO, and Nb_2O_5 pastes, respectively, were prepared by homogenizing each sample with ethylcellulose (SDFCL) and anhydrous α-terpineol (Kemphasol Ltd., India) as follows. First, the respective TiO_2, ZnO, and Nb_2O_5 nanopowders and ethylcellulose were introduced to a mortar and continuously ground for 15 min while adding ethanol (Changshu, China) gradually. Each mixture was then homogenized for 2 h in an ultrasonic bath before adding α-terpineol. Two to three drops of acetylacetone (HPCL, India) were added to the (TiO_2, ZnO, and Nb_2O_5) dispersions, and homogenization was carried out in an ultrasonic bath for 3 h.[36,63,67]

2.2. Preparation of TiO_2, ZnO, and Nb_2O_5 Photoanodes and Fabrication of DSSCs. Using the chemical bath deposition technique (CBD), the compact TiO_2 layer was first deposited before the porous (TiO_2 and Nb_2O_5) layer, as similarly reported.[73,74] Before the porous (ZnO) layer was deposited, the compact ZnO layer was prepared using successive ionic layer adsorption and reaction (SILAR) techniques similarly reported.[37] The as-deposited compact ZnO and TiO_2 film was annealed at 450 °C for 1 h. Compact TiO_2-deposited FTO (fluorine-doped tin oxide) deposits a porous layer of (TiO_2 and Nb_2O_5), while compact ZnO-deposited FTO deposits a porous layer of (ZnO). On compact TiO_2-deposited FTO, (TiO_2 and Nb_2O_5) paste was coated; in compact ZnO-deposited FTO, (ZnO) paste was coated using the Doctor blade method. All the (TiO_2, ZnO, and Nb_2O_5) photoanodes were dried using an incubator and air-annealed at 450 °C for 1 h.

0.05 M NO_2Lw solutions were prepared in ethanol, and the annealed (TiO_2, ZnO, and Nb_2O_5) photoanode were immersed for 72 h. This (TiO_2, ZnO, and Nb_2O_5) photoanode was utilized to fabricate DSSCs after photosensitizer loading.

A 4 μm spacer was added between the platinum-coated FTO counter electrode and the (TiO_2, ZnO, and Nb_2O_5) photoanode to avoid direct contact. The redox electrolyte solution was utilized as a liquid electrolyte. It contained 0.5 M lithium iodide (SRL, India), 0.05 M iodine (Fisher Scientific, USA), and 0.5 M tertiary butylpyridine (ACROS Organics, Belgium) solution in acetonitrile (SDFCL, India, used as received).[36]

2.3. Characterization. By using X-ray diffraction (Bruker D8, with Cu Kα λ = 0.154 nm) at 20−80°, the crystal structure and crystalline size of the photoanodes were studied. JEM-2010 field emission scanning electron microscopy (FE-SEM) (SUPRA40VP, Germany) was employed to examine the surface morphologies of photoanodes. The shape and size of TiO_2 ZnO, and Nb_2O_5 nanoparticles and selective area electron diffraction (SAED) patterns were studied using transmission electron microscopy (TEM) (TECNAI 12 G2 TEM). X-ray photoelectron spectroscopy analysis of TiO_2, ZnO, and Nb_2O_5 and NO_2Lw-loaded TiO_2, ZnO, and Nb_2O_5 was used to characterize the elemental composition with chemical states (XPS: M/s Thermo Fisher Scientific Instrument UK, K Alpha +) with Al Kα monochromator radiation at 12 kV and 6 mA beam current. The UV−visible absorption spectra of the photosensitizer were measured (SHIMADZU UV 1650), and emission spectra were obtained using a spectrofluorometer (JASCO FP-8300). The Fourier-transform infrared spectroscopy (FT-IR) spectra of NO_2Lw and the NO_2Lw-loaded TiO_2 ZnO, and Nb_2O_5 photoanode were measured (BRUKER VERTEX by SHIMADZUFT 8400 Spectrometer). The Raman spectra are recorded by Renishaw with a He−Ne laser at 785 nm as the excitation source. Using CH equipment with an electrochemical analyzer (CHI 6054E), the photosensitizer cyclic voltammetry (CV) measurement was carried out in ethanol as the solvent. Using a potentiostat (Vertex IVIUM Technologies Netherlands), EIS measurement performs over the frequency range of 10^6−10^0 under dark illumination at the voltage that corresponds to open-circuit voltage. Keithley 2400 source meter and solar simulator (ENLITECH model SS-F5−3A) were used to analyze the photocurrent density−voltage (J−V) characteristic curve of the fabricated DSSCs under 100 mW/cm^2 illumination.

2.4. Synthesis of NO_2Lw (2-Hydroxy-3-nitronaphthalene-1,4-dione). Using Scheme 1, NO_2Lw (2-hydroxy-3-nitronaphthalene-1,4-dione) was synthesized. This procedure involved dissolving 0.03 mol (6.81 g) of dichlone (2,3-dichloronaphthalene-1,4-dione) in 38 mL of methanol and 0.10 mol (6.90 g) of sodium nitrite ($NaNO_2$) in 52 mL of water and mixing both solutions in a round-bottom flask. The mixture was warmed at 70 °C continuously for 2.5 h. After heating the solution, the mixture was kept aside for 1 h. A red-colored precipitate was formed, which was then dissolved in warm water. After the reaction mixture was neutralized with 2 N hydrochloric acid, a residue of NO_2Lw (2-hydroxy-3-nitronaphthalene-1,4-dione), which was yellow, was produced.[75]

Scheme 1. Synthesis of NO_2Lw (2-Hydroxy-3-nitronaphthalene-1,4-dione)

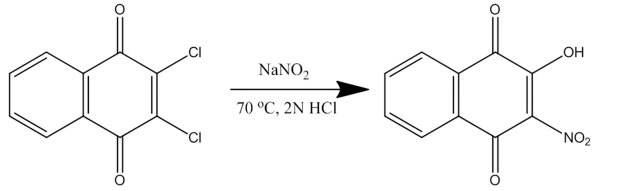

2,3-dichloronaphthalene-1,4-dione 2-hydroxy-3-nitronaphthalene-1,4-dione

https://doi.org/10.1021/acsomega.3c06271
ACS Omega 2023, 8, 38748−38765

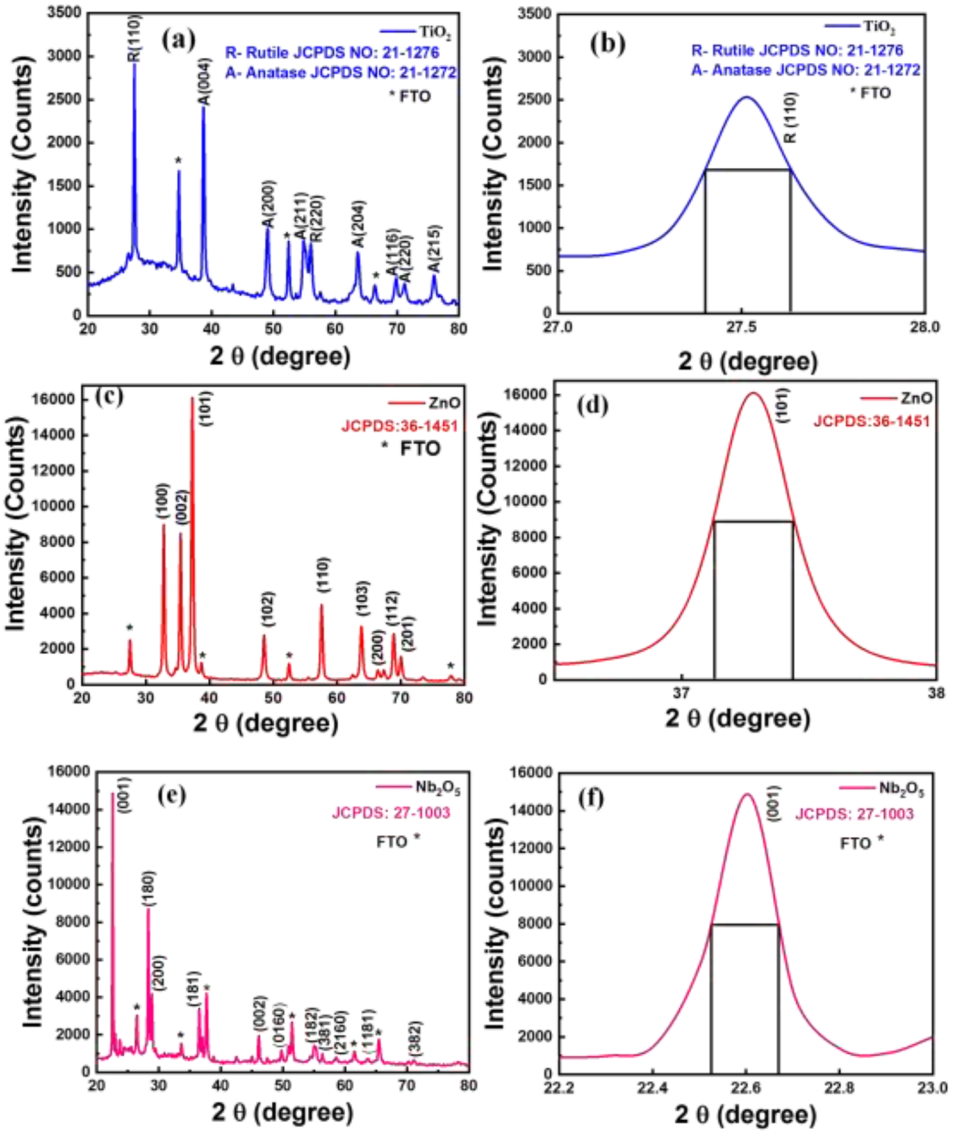

Figure 2. X-ray diffraction patterns and crystallite size calculation of (a, b) TiO_2, (c, d) ZnO, and (e, f) Nb_2O_5 photoanodes.

3. RESULT AND DISCUSSION

3.1. Structural Properties of TiO_2, ZnO, and Nb_2O_5 Photoanode. The TiO_2, ZnO, and Nb_2O_5 photoanode crystal structure and crystalline size were determined using the X-ray diffraction pattern, as shown in Figures 2a/b, c/d, and e/f, respectively.

The TiO_2 photoanode deposited on FTO is depicted in Figure 2a/b with its X-ray diffraction pattern and the full width at half-maximum (fwhm) of (110) peaks. The obtained XRD pattern was compared to the standard data, and it was found that the crystal planes of the anatase phase were confirmed by comparison with JCPDS card no. 21−1272, while the rutile phase[76] was verified by comparison with JCPDS card no. 21−1276. The Scherrer formula[77,78] was used to determine the crystallite size of TiO_2. The crystallite size of the TiO_2 was determined to be ∼37 nm.

The X-ray diffraction patterns and the fwhm of (101) peaks of the ZnO photoanode deposited on FTO are displayed in Figure 2c/d. The obtained XRD pattern was compared to the available data and found to match the JCPDS card no. 36−1451 for ZnO, confirming the formation of the wurtzite structure showing a hexagonal phase for ZnO.[79] The crystallite size of the ZnO was found to be ∼52 nm.

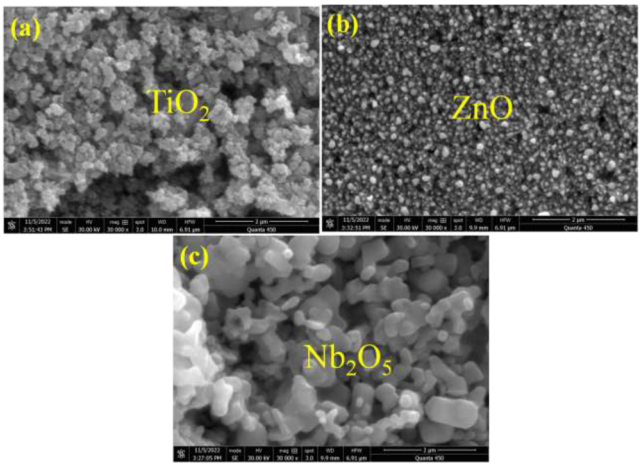

Figure 3. Surface morphology of (a) TiO_2, (b) ZnO, and (c) Nb_2O_5 photoanodes.

https://doi.org/10.1021/acsomega.3c06271
ACS Omega 2023, 8, 38748−38765

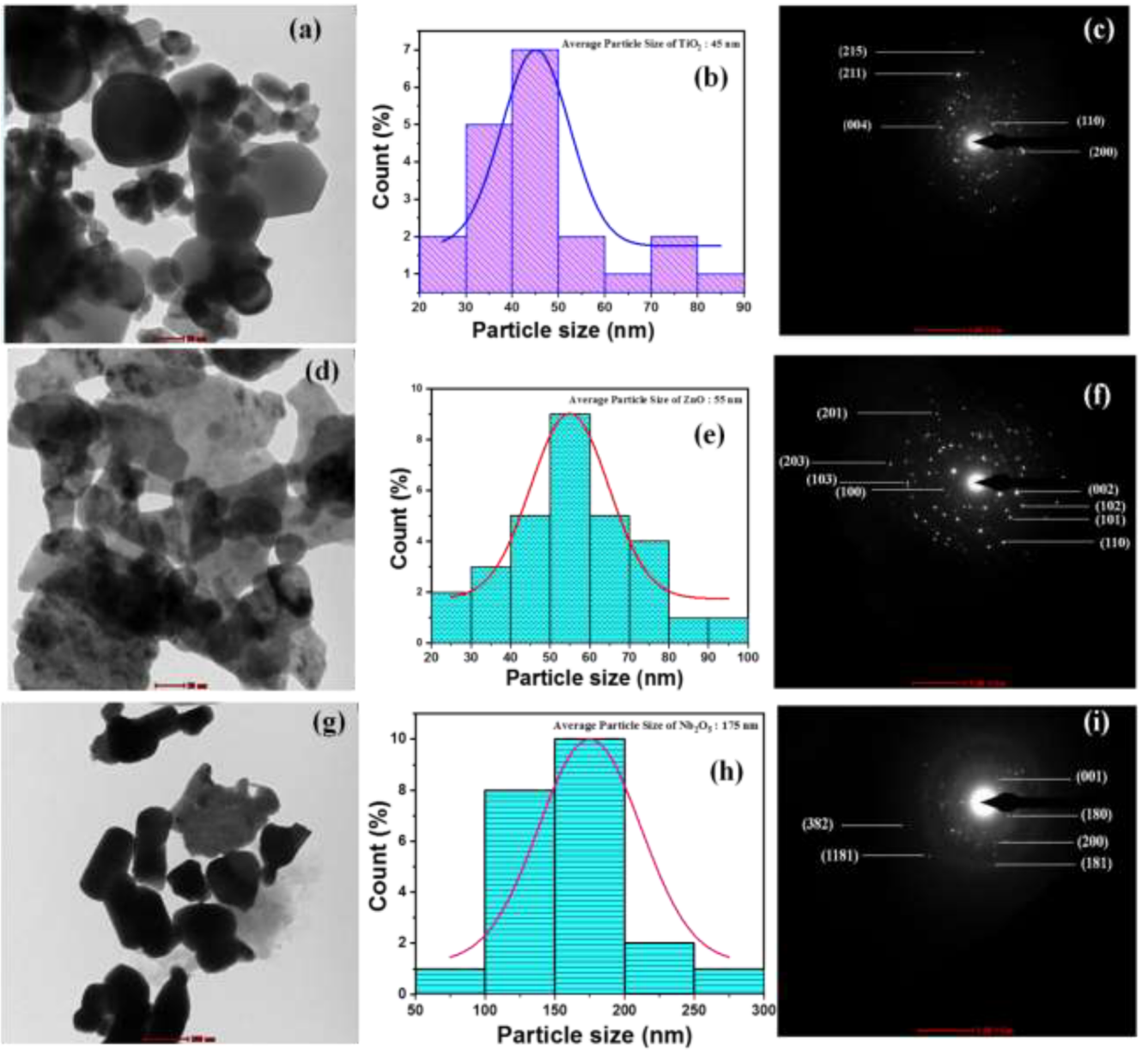

Figure 4. (a, d, g) TEM micrographs, (b, e, h) particle size histogram, and (c, f, i) selective area electron diffraction pattern of TiO_2 nanoparticles, ZnO nanoparticles, and Nb_2O_5 submicron-particles, respectively.

The Nb_2O_5 photoanode deposits on FTO are depicted in Figure 2e/f, which shows the X-ray diffraction patterns and the fwhm of (001) peaks. According to JCPDS card no. 27−1003, the orthorhombic structure of the Nb_2O_5 photoanode is confirmed by its X-ray diffraction patterns.[80,81] The crystallite size of the Nb_2O_5 was found to be ∼56 nm.

3.2. Morphological Surface Analysis of TiO_2, ZnO, and Nb_2O_5 Photoanodes. The FE-SEM technique was used to examine the surface morphologies of the TiO_2, ZnO, and Nb_2O_5 photoanodes. FE-SEM images of TiO_2, ZnO, and Nb_2O_5 photoanodes are shown in Figure 3a−c. The spherical shape and porous morphology of the high-density TiO_2 clusters are depicted in Figure 3a. The TiO_2 photoanode porous structure boosts the quantity of photosensitizer loading by offering a high surface area resulting in increased fabricated device efficiency.[66,82−84] The ZnO photoanode surface morphology shown in Figure 3b, deposited by using the Doctor blade technique, exhibits uniformly distributed nanograins with porous morphology. Pores of submicrometer size are seen to be evenly dispersed across the entire ZnO photoanode surface. Since light harvesting efficiency depends on the amount of efficient photosensitizer adsorbed on the photoanode surface,[68] ZnO photoanode's porous characteristic is crucial to achieving improved light harvesting.[85,86] Figure 3c FE-SEM image shows the surface morphology of the Nb_2O_5 photoanode presented. The Nb_2O_5 photoanode deposited by the Doctor blade technique reveals irregular spherical particles of well-defined shape.[87−90]

The porosity observed in the TiO_2, ZnO, and Nb_2O_5 photoanodes facilitates the adsorption of NO_2Lw molecules, which allows the photosensitizer molecules to penetrate the porous TiO_2, ZnO, and Nb_2O_5 photoanode so that they get attached to the interfacial surface.[91−93]

https://doi.org/10.1021/acsomega.3c06271
ACS Omega 2023, 8, 38748−38765

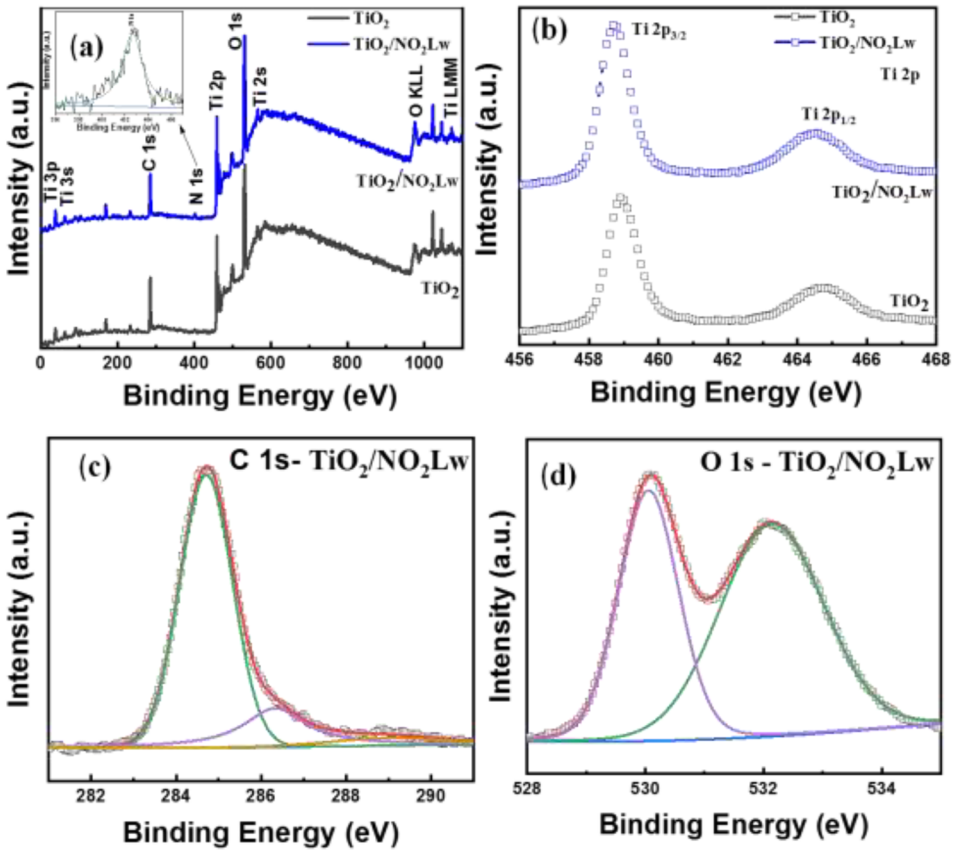

Figure 5. (a) XPS survey spectra and (b) core level XPS spectra of Ti 2p of TiO_2 and TiO_2/NO_2Lw photoanodes. Core level XPS spectra of (c) C 1s and (d) O 1s of TiO_2/NO_2Lw photoanode.

3.3. Transmission Electron Microscopy (TEM). Figure 4a−i displays TEM micrographs, particle size histograms, and selective area electron diffraction (SAED) patterns of TiO_2 nanoparticles (Figure 4a−c), ZnO nanoparticles (Figure 4d−f), and Nb_2O_5 submicron-particles (Figure 4g−i).

Figure 4a/d/g shows a TEM micrograph of TiO_2, ZnO, and Nb_2O_5 with spherical TiO_2 particles.[94] In the instance of ZnO, it was found to have agglomerated nanoparticles,[95] whereas Nb_2O_5 contains irregular submicron-particles.[96] Figure 4b/e/h depict the particle size distribution histogram of TiO_2, ZnO, and Nb_2O_5 fitted to Gaussian distribution. According to the histogram, the average particle size for TiO_2 and ZnO nanoparticles was 45 and 55 nm, respectively, whereas Nb_2O_5 submicron-particles were 175 nm. TiO_2 has a lower average particle size than ZnO and Nb_2O_5. The smaller the nanoparticles, the greater the surface area and the photosensitizer adsorption capacity of the photoanode material.[97] Compared with ZnO and Nb_2O_5, the TiO_2 photoanode exhibits more NO_2Lw photosensitizer adsorption. The polycrystalline nature of TiO_2, ZnO, and Nb_2O_5 was deduced from the SAED pattern, which reveals the characteristic ring pattern (Figure 4 c/f/i). Using SAED, the *d*-spacing values of TiO_2, ZnO, and Nb_2O_5 are computed, and the estimated *d*-spacing value corresponds with the XRD result.[98−100]

3.4. X-ray Photoelectron Spectroscopy. X-ray photoelectron spectroscopy (XPS) technique was used to analyze the chemical and electronic states of the elements found in TiO_2, ZnO, and Nb_2O_5 as photoanode materials, as well as NO_2Lw-loaded TiO_2, ZnO and Nb_2O_5 photoanodes. The survey spectra displayed in Figure 5a for both TiO_2 and TiO_2/NO_2Lw photoanodes exclusively reveal the existence of Ti, O, and C elements, with TiO_2/NO_2Lw showing extra N element.

The inset of Figure 5a depicts the spectrum of N 1s observed at 402.65 eV, which exhibits nitrogen peaks attributed to the nitro group present.[101] The binding energy (BE) values for Ti $2p_{1/2}$ and Ti $2p_{3/2}$ were 464.6 and 458.9 eV for TiO_2 and 464.5 and 458.7 eV for TiO_2/NO_2Lw, respectively, according to the Ti 2p core level spectra shown in Figure 5b, and these two peaks in TiO_2 and TiO_2/NO_2Lw correspond to the Ti^{4+} of TiO_2.[102] Figure 5c and d shows the C 1s and O 1s spectra of the TiO_2/NO_2Lw photoanode. XPSPEAK 41 software was used for fitting and background subtraction. The main peak in the C 1s spectrum at 284.8 eV is attributed to the sp^2-hybridized carbon atom fitted by three peaks: the two at 284.70 and 286.35 corresponding to C═C and C−O bonds, and the less intense broader peak near 289.10 eV that is due to the C═O group[103] present in the NO_2Lw molecule observed for the TiO_2/NO_2Lw photoanode as shown in Figure 5c. The two peaks at 530.05 and broad peaks around 532.15 in the O 1s spectrum from Figure 5d are ascribed to the TiO_2 lattice oxygen and C═O oxygens in the absorbed NO_2Lw molecule.[104] The XPS study spectra show Ti is present at a +4 oxidation in a state with oxygen vacancies, allowing an acceptable quantity of NO_2Lw absorption into the TiO_2 photoanode.

The ZnO and ZnO/NO_2Lw photoanodes XPS was carried out, and the result is shown in Figure 6. The survey scan spectrum in Figure 6a shows that ZnO and ZnO/NO_2Lw photoanodes confirm the presence of Zn, O, and C element, and ZnO/NO_2Lw shows the addition of N element. The inside

https://doi.org/10.1021/acsomega.3c06271
ACS Omega 2023, 8, 38748−38765

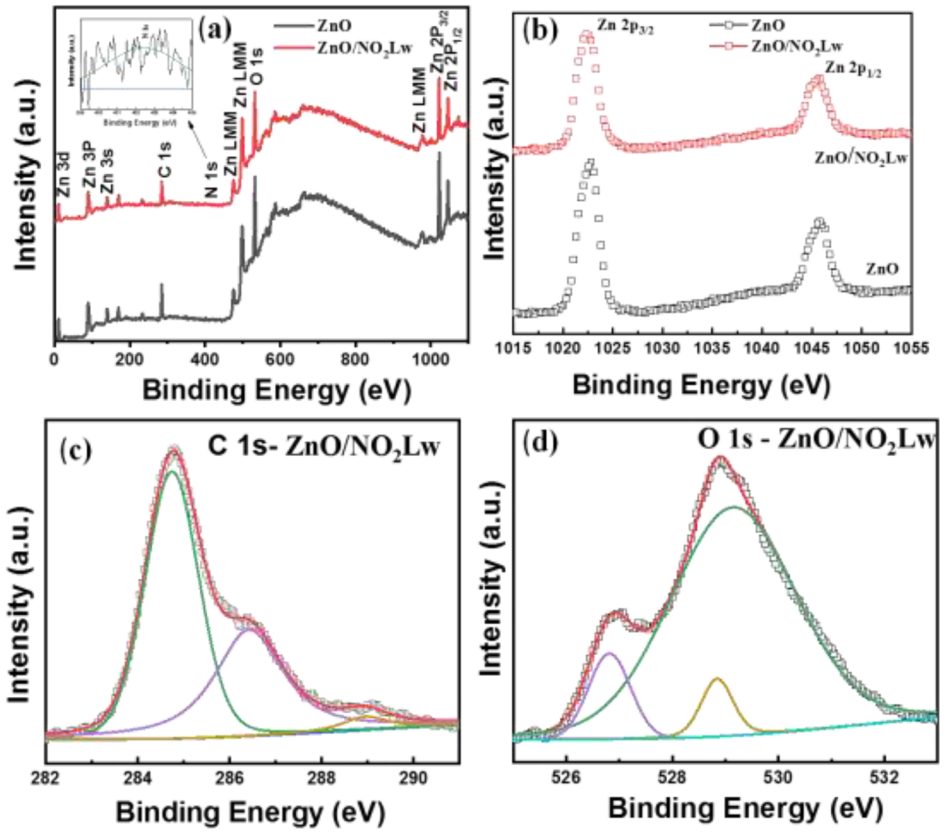

Figure 6. (a) XPS survey spectra and (b) core level XPS spectra of Zn 2p of ZnO and ZnO/NO_2Lw photoanodes. Core level XPS spectra of (c) C 1s and (d) O 1s of ZnO/NO_2Lw photoanode.

of Figure 6a depicts the spectrum of N 1s observed at 402.4 eV.[101] The Zn 2p consists of two peaks, Zn $2p_{1/2}$ and Zn $2p_{3/2}$ positioned at 1045.7 and 1022.75 eV for the ZnO and 1045.75 and 1022.5 eV[105] for the ZnO/NO_2Lw, as shown Figure 6b, which were observed for both ZnO and ZnO/NO_2Lw. The binding energy differences between Zn $2p_{1/2}$ and Zn $2p_{3/2}$ for the ZnO and ZnO/NO_2Lw was 22.95 and 23.25 eV, the characteristic value of ZnO.[106]

Figure 6c shows that the C 1s can be fitted by three peaks at 284.75, 286.45, and 289 eV corresponding to C═C and C−O bonds ZnO/NO_2Lw. The less intense broader peak near 289 eV is due to the C═O[103] group in the NO_2Lw molecule observed for the ZnO/NO_2Lw photoanode. Figure 6d shows that the O 1s was fitted using XPSPEAK 41 software by three nearly peaks in the ZnO/NO_2Lw photoanode, indicating three different O species in the ZnO/NO_2Lw photoanode. The lowest binding energy peaks at 526.8 eV are attributed to oxygen at the lattice site.[106] The middle binding energy, 528.85 eV, is attributed to chemically adsorbed oxygen on the surface[107] of NO2Lw. The highest component is attributed to interstitial oxygen in ZnO.[106]

Nb_2O_5 and Nb_2O_5/NO_2Lw photoanodes were analyzed using XPS. Figure 7a depicts the XPS survey spectra of the Nb_2O_5 and Nb_2O_5/NO_2Lw photoanodes. Figure 7a inset shows the core level spectrum of N 1s observed at 403.05 eV.[101] The core level XPS spectra of Nb 3d of the Nb_2O_5 and Nb_2O_5/NO_2Lw photoanodes are shown in Figure 7b. The BE values for the Nb $3d_{3/2}$ and Nb $3d_{5/2}$ were, respectively, 210.35 and 207.65 eV for the Nb_2O_5 and 209.95 and 207.25 eV for the Nb_2O_5/NO_2Lw; these two peaks in Nb_2O_5 and Nb_2O_5/NO_2Lw correlate to pentavalent niobium.[108] The core level XPS spectra of C 1s are shown in Figure 7c. The sp^2-hybridized carbon atom is responsible for the main peak in the C 1s spectrum at 284.8 eV. The C 1s peak is fitted by three peaks at 284.85, 285.55, and 286.45 eV corresponding to C═C, C−O, and C═O bonds.[103] These functional groups facilitate the formation of chemical bonds in the Nb_2O_5 lattice. Figure 7d depicts the core level XPS spectra of O 1s from an Nb_2O_5/NO_2Lw photoanode. The three peaks occurring at 527.35 and 529 eV, and wide peaks at 528.9 correspond to the lattice oxygen in the Nb_2O_5 and C═O oxygens[104] in the absorbed NO_2Lw molecules.

3.5. Raman Spectra. Raman spectra of TiO_2, Nb_2O_5, and NO_2Lw-loaded TiO_2 and Nb_2O_5 photoanodes are shown in Figure 8. The characteristic Raman absorption bands centered at 138, 194, 395, 516, and 636 cm^{-1} are attributed to TiO_2[103] phonon modes, as illustrated in Figure 8a, and the characteristic Raman absorption bands centered at 124, 236, 312, 500, 690, 734, and 935 cm^{-1} are attributed to the phonon modes of Nb_2O_5,[109] as illustrated in Figure 8b. When compared to the Raman spectrum of the TiO_2 and Nb_2O_5, the Raman spectra of NO_2Lw-loaded TiO_2 and Nb_2O_5 contain more NO_2Lw photosensitizer NO_2-group-derived bands (e.g., at 1336 and 1335 cm^{-1}).[110] Raman spectra verified the highly ordered TiO_2 and Nb_2O_5 photoanodes, their functionalization via the changes in intensities of the NO_2Lw-loaded TiO_2 and Nb_2O_5 photoanodes, and the interaction between the NO_2Lw molecule and TiO_2 and Nb_2O_5 photoanodes.[111]

3.6. Emission Studies. The photoluminescence (PL) spectra of TiO_2, ZnO, and Nb_2O_5 with deconvoluted PL spectra are shown in Figures 9 a, b, and c, respectively. The emission spectra of TiO_2, ZnO, and Nb_2O_5 photoanodes have

https://doi.org/10.1021/acsomega.3c06271
ACS Omega 2023, 8, 38748−38765

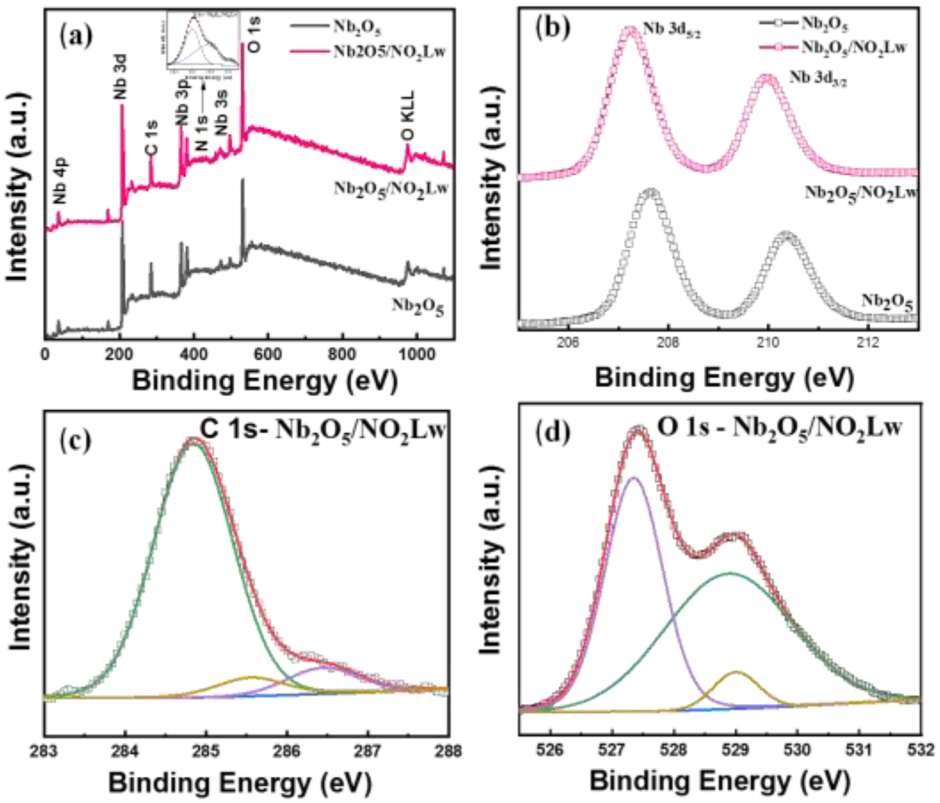

Figure 7. (a) XPS survey spectra and (b) core level XPS spectra of Nb 3d of Nb_2O_5 and Nb_2O_5/NO_2Lw photoanodes. Core level XPS spectra of (c) C 1s and (d) O 1s of Nb_2O_5/NO_2Lw photoanode.

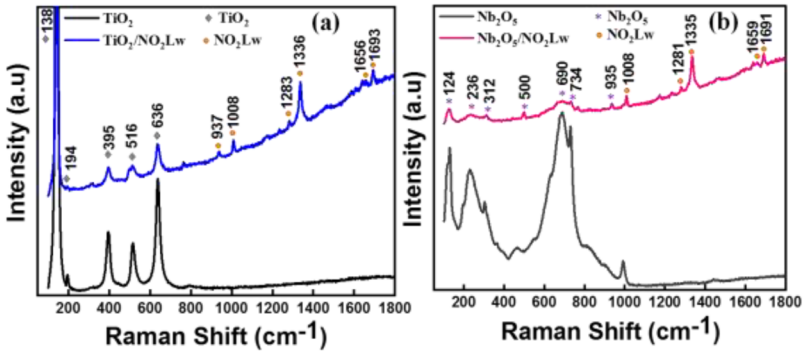

Figure 8. Raman spectra of (a) TiO_2 and NO_2Lw-loaded TiO_2 photoanodes and (b) Nb_2O_5 and NO_2Lw-loaded Nb_2O_5 photoanodes.

been studied to investigate radiative and nonradiative recombination surface characteristics and defect states.[112] Figure 9a, b, and c shows two emission bands in TiO_2, ZnO, and Nb_2O_5. The second emission band in TiO_2, ZnO, and Nb_2O_5 PL emission spectra represents green emission caused by oxygen vacancies and surface defects. The green emission is quite strong because of radial recombination between photogenerated holes with trap electrons at the oxygen vacancies.[113−116]

3.7. UV−visible Absorbance of NO_2Lw, Photoanodes (TiO_2/NO_2Lw, ZnO/NO_2Lw, Nb_2O_5/NO_2Lw), and Fluorescence Spectra Measurement of NO_2Lw. Figure 10a, b depicts the UV−visible absorbance spectra of NO_2Lw and NO_2Lw-loaded TiO_2, ZnO, and Nb_2O_5 photoanodes.

The UV−visible absorbance for NO_2Lw in ethanolic solutions is depicted in Figure 10a as a function of wavelength. NO_2Lw was found to have absorptions ranging from 310 to 540 nm. The substituted nitro group electron delocalization effect shows the charge transfer band in NO_2Lw. The UV−visible absorbance spectra of NO_2Lw demonstrate the absorption ascribed to ultraviolet and visible region charge transfer. NO_2Lw has a maximum absorption wavelength (λ_{max}) of ∼391 nm.

Figure 10b shows the optical absorbance spectra of the NO_2Lw-loaded TiO_2, ZnO, and Nb_2O_5 photoanodes. The maximum absorption wavelength (λ_{max}) is exhibited at 439, 438, and 427 nm for NO_2Lw-loaded TiO_2, ZnO, and Nb_2O_5 photoanodes, respectively. The NO_2Lw-loaded TiO_2, ZnO, and Nb_2O_5 photoanodes show the redshift in the visible region, confirming the formation of complexation between NO_2Lw and TiO_2, ZnO, and Nb_2O_5 photoanodes, which

https://doi.org/10.1021/acsomega.3c06271
ACS Omega 2023, 8, 38748−38765

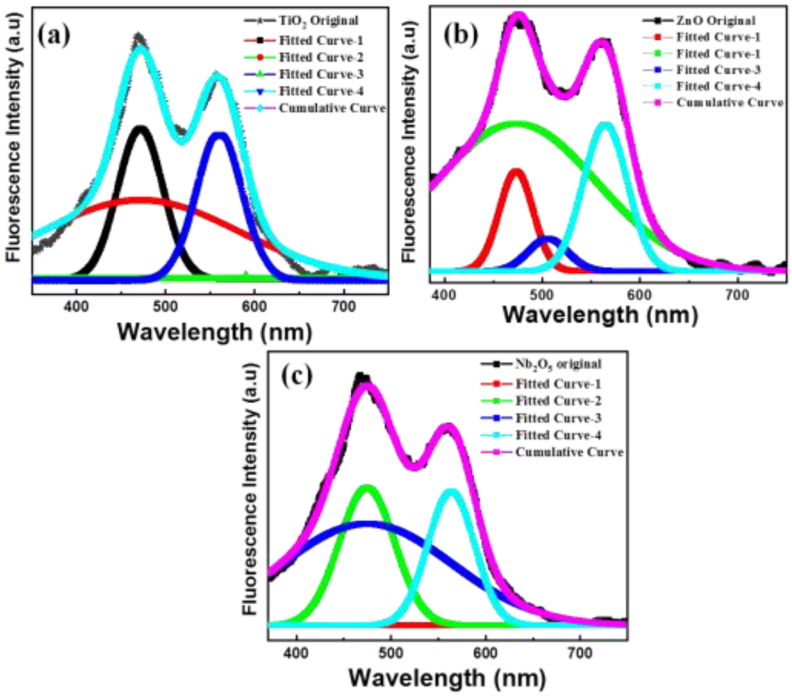

Figure 9. Photoluminescence (PL) spectra of (a) TiO_2, (b) ZnO, and (c) Nb_2O_5 with deconvoluted PL spectra.

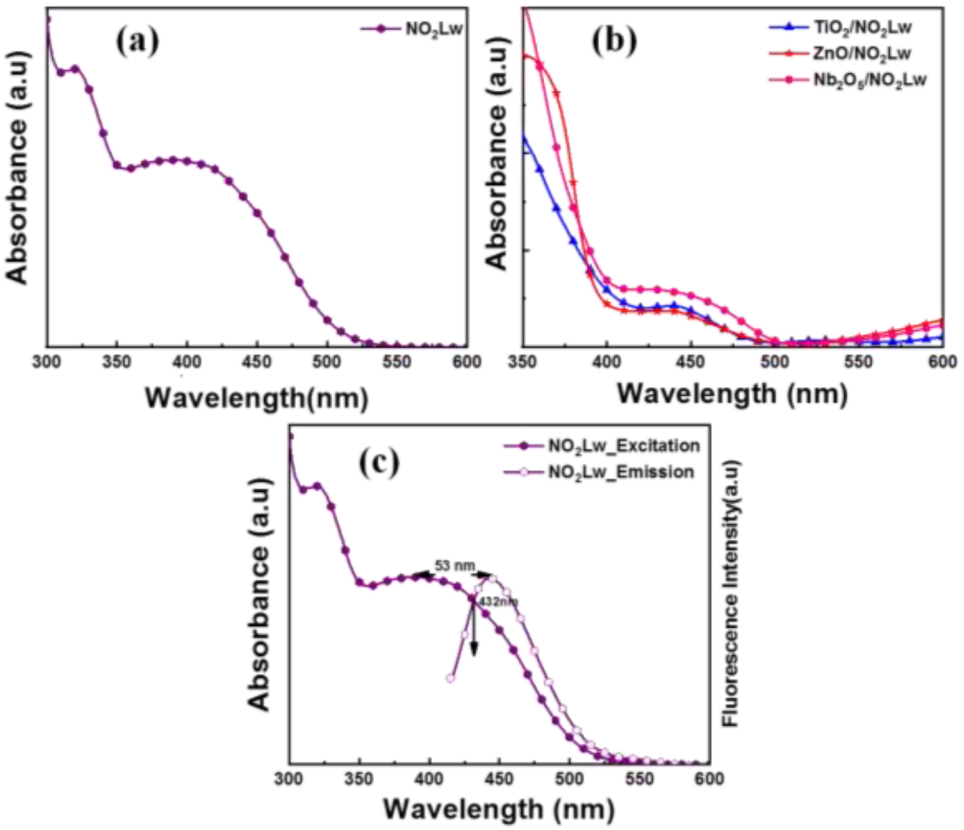

Figure 10. UV−visible spectra of (a) NO_2Lw and (b) NO_2Lw-loaded TiO_2, ZnO, and Nb_2O_5 photoanodes. (c) Combination of UV−visible (excitation) and fluorescence (emission) spectra of NO_2Lw.

demonstrates the sufficient amount of photosensitizer adsorbed on the TiO_2, ZnO, and Nb_2O_5 surfaces.[117,118]

Figure 10c depicts the combined UV−visible (excitation) and fluorescence (emission) spectra of the NO_2Lw. The fluorescence (emission) spectra were measured, and the fluorescence emission maxima (λ_{PL}) value is displayed in Table 2. It exhibits fluorescence emission maxima at (λ_{PL}) ~444 nm, and the stock shift for NO_2Lw is 53 nm. The

https://doi.org/10.1021/acsomega.3c06271
ACS Omega 2023, 8, 38748−38765

Table 2. Photophysical and Electrochemical Data of NO_2Lw

Photosensitizer	λ_{max} (nm)	λ_{PL} (nm)	Stokes shift (nm)	E_{0-0} (eV)	E_{HOMO} (eV)	E_{LOMO} (eV)
NO_2Lw	391	444	53	2.87	−6.73	−3.86

combination of UV−visible (excitation) and fluorescence (emission) spectra of NO_2Lw helps to calculate energy difference,[80,81] i.e., the E_0-E_0 (E_{0-0}) difference of NO_2Lw using the formula,

$$E = h \times \nu = \frac{h \times c}{\lambda} = \frac{1240}{\lambda} \quad (1)$$

Where E is the energy difference in eV, h represents the Planks constant, λ represents the intersection of excitation and emission spectra in nm, and c is the speed of light. The E_{0-0} of the NO_2Lw is calculated and equals 2.87 eV.[119,120]

3.8. Electrochemical Characterization Using Cyclic Voltammetry. Figure 11a depicts the NO_2Lw cyclic voltammogram in an ethanol solution. The highest occupied molecular orbital (HOMO) and lowest unoccupied molecular orbital (LUMO) energy levels were calculated using the cyclic voltammeter (CV) approach.

As shown in Figure 11a, the first reduction potential (onset of the first reaction peak) can be used to compute the LUMO.[121,122] The NO_2Lw has an E_{LUMO} of −3.86 eV. The E_{HOMO} is −6.73 eV and was calculated using the E_{LUMO} and the E_{0-0} values. Table 2 displays the electrochemical and optoelectrical parameters. Figure 11b depicts the energy level diagram of the NO_2Lw and the conduction band edge of the TiO_2, ZnO, and Nb_2O_5 photoanodes. TiO_2 and ZnO have conduction bands below the NO_2Lw LUMO level, but Nb_2O_5 has a conduction band above the NO_2Lw LUMO level. Iodine/triiodide has a redox potential (−4.8 eV)[123] above the HOMO level of NO_2Lw. It is possible to regenerate photosensitizers in TiO_2, ZnO, and Nb_2O_5-based DSSCs with a driving force of ∼1.93 eV, which is sufficient.

3.9. FT-IR Analysis. Figure 12a−c displays the FTIR spectra of NO_2Lw and NO_2Lw-loaded TiO_2, ZnO, and Nb_2O_5 photoanodes. When NO_2Lw-loaded TiO_2, ZnO, and Nb_2O_5 photoanodes were compared to NO_2Lw, the bonding interaction[124,125] was visible in the frequency range of NO_2Lw-loaded TiO_2, ZnO, and Nb_2O_5 photoanodes. Table 3 summarizes the characteristics of the frequency band of NO_2Lw and photosensitizer-loaded TiO_2, ZnO, and Nb_2O_5 photoanodes. The stretching frequency of the NO_2 group is attributed to the bands in the NO_2Lw FTIR spectra that are in the range of 1597 cm^{-1} (antisymmetrical) and 1312 cm^{-1} (symmetrical).[75] Figure 12a−c depicts the increase in the NO_2 stretching frequency at the photosensitizer-loaded TiO_2, ZnO, and Nb_2O_5 photoanodes from 1312 cm^{-1} to 1323, 1325, and 1327 cm^{-1}, respectively. Due to the frequency of hydroxyl group (O−H) stretching, the peak occurred at 3563 and 3516 cm^{-1}, as illustrated in Figure 12a−c. One band is visible in photoanodes made of TiO_2, ZnO, and Nb_2O_5 that have been loaded with photosensitizer after coordination[126] at 3324, 3334, and 3321 cm^{-1}, respectively

In photoanodes with photosensitizer-loaded TiO_2, ZnO, and Nb_2O_5, the $\nu_{C=O}$ frequencies of NO_2Lw detected at 1692 cm^{-1} after coordination are shifted to lower frequencies 1657, 1652, and 1648 cm^{-1}, respectively.[120,127] TiO_2, ZnO, and Nb_2O_5 are attached to the NO_2Lw anchoring site via ν_{OH} and $\nu_{C=O}$ bonding. The band observed at 1001 cm^{-1} that was noticed as a result of photosensitizers ν_{C-O} stretching frequency of NO_2Lw is shifted to 1042 cm^{-1} in photosensitizer-loaded TiO_2, ZnO, and Nb_2O_5 photoanode after coordination, indicating a significant interaction between the NO_2Lw and TiO_2, ZnO, and Nb_2O_5 photoanodes that serves to generate a chain-like structure for the device's facile electrons transfer.

3.10. Solar Cell Characterization. In comparison to TiO_2, ZnO, and Nb_2O_5, which have conduction bands (CBs) at −4.25, −4.0, and −3.7 eV, respectively, NO_2Lw has the LUMO level at −3.86 eV. Thus, based on the energy levels of NO_2Lw, TiO_2, and ZnO, the electron injection from the LUMO level of NO_2Lw into the CB of TiO_2 and ZnO is possible. However, the CB position of Nb_2O_5 (−3.7 eV)[36] is above the LUMO level of NO_2Lw (−3.86 eV). Some unexpected electron injection has been observed in the present case, and Nb_2O_5 photoanode-based DSSCs[128,129] showed lower performance than ZnO and TiO_2.

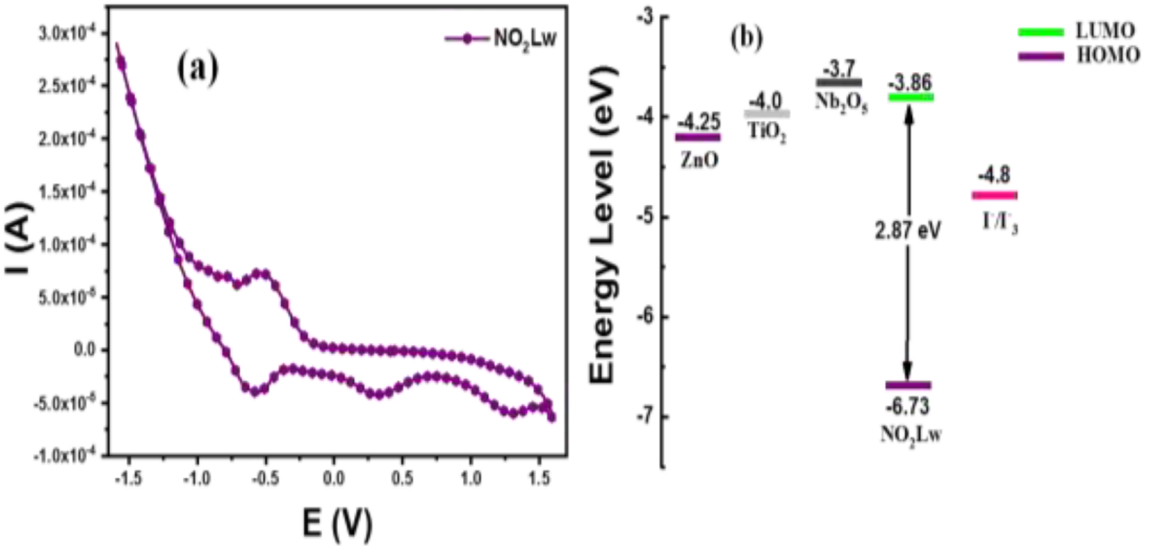

Figure 11. (a) Cyclic voltammograms of NO_2Lw. (b) HOMO−LUMO comparison plot with conduction bands of TiO_2, ZnO, and Nb_2O_5 and redox potential of I^-/I_3^-.

https://doi.org/10.1021/acsomega.3c06271
ACS Omega 2023, 8, 38748−38765

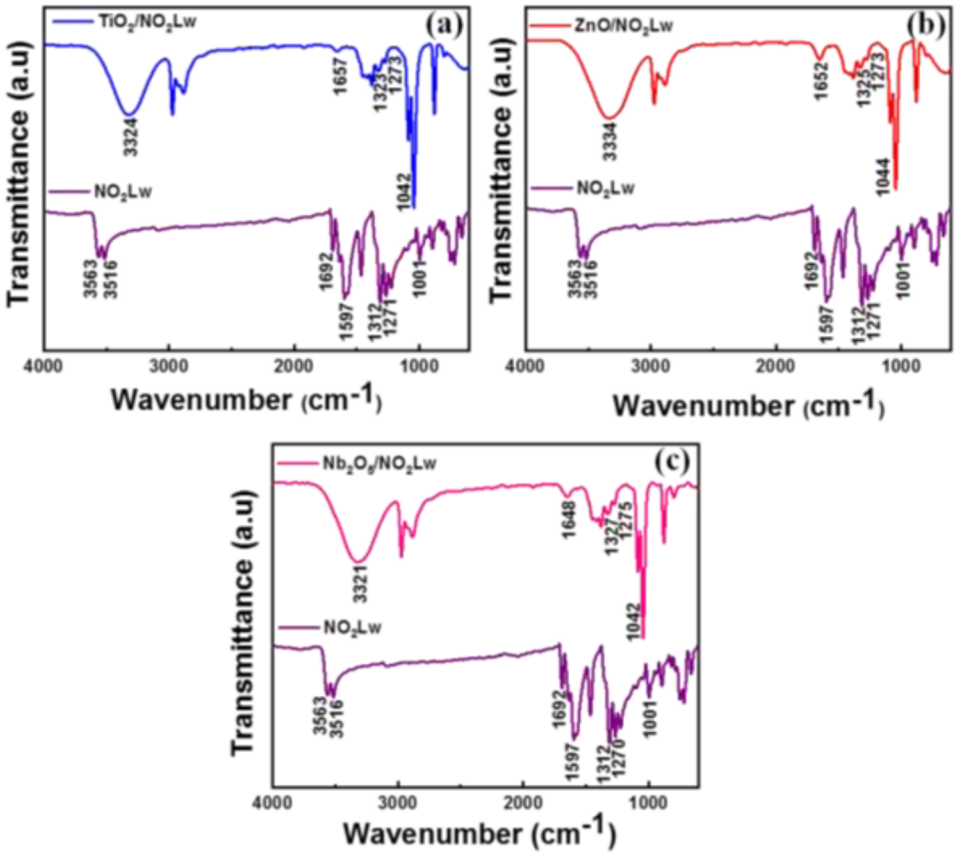

Figure 12. FT-IR spectra of (a) NO_2Lw and NO_2Lw-loaded TiO_2 photoanodes, (b) NO_2Lw and NO_2Lw-loaded ZnO photoanodes, and (c) NO_2Lw and NO_2Lw-loaded Nb_2O_5 photoanodes.

Table 3. Selected FT-IR Frequencies of the NO_2Lw and NO_2Lw-loaded TiO_2, ZnO, and Nb_2O_5 Photoanodes

Photosensitizer/ Photoanode	ν_{O-H} (cm^{-1})	$\nu_{C=O}$ (cm^{-1})	ν_{N-O} (cm^{-1})	ν_{C-C} (cm^{-1})	ν_{C-O} (cm^{-1})
NO_2Lw	3563, 3516	1692	1597, 1312	1271	1001
TiO_2/NO_2Lw	3324	1657	1323	1273	1042
ZnO/NO_2Lw	3334	1652	1325	1273	1042
Nb_2O_5/NO_2Lw	3321	1648	1327	1275	1042

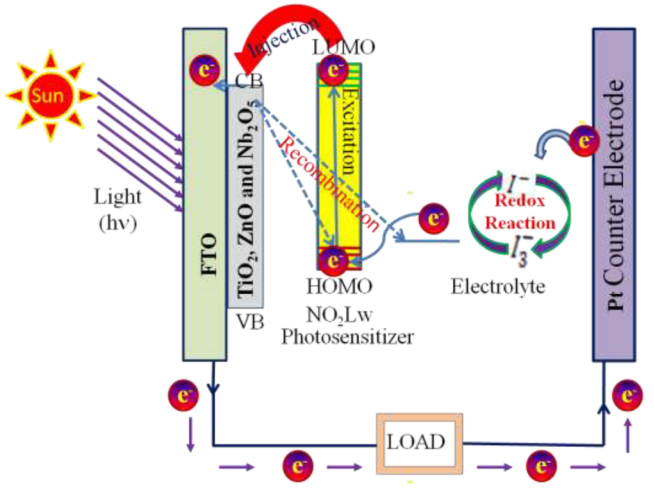

Figure 13. Schematic of the process embedded in DSSCs.

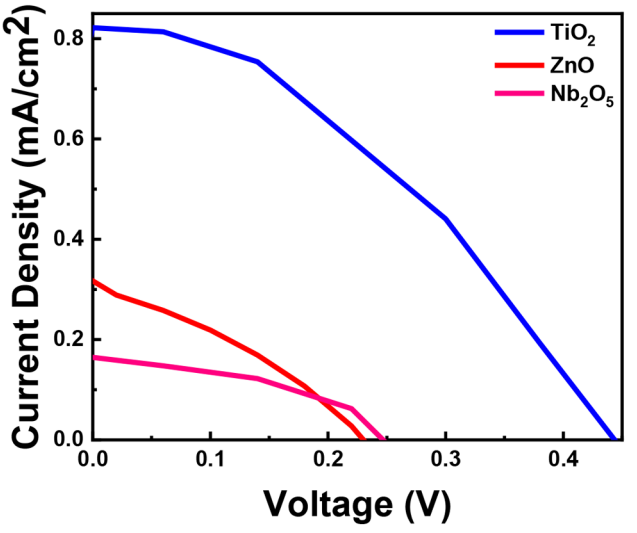

Figure 14. $J-V$ plot characteristic of TiO_2, ZnO, and Nb_2O_5 photoanode-based devices.

Figure 13 depicts a schematic of the process flow for NO_2Lw-sensitized TiO_2, ZnO, and Nb_2O_5-based DSSCs. The photon incident excites the electron at the NO_2Lw, injecting the excited electron into the respective CB of TiO_2, ZnO, and Nb_2O_5. The NO_2Lw HOMO level (−6.73 eV) is below the iodine/triiodide electrolyte redox potential (−4.8 eV), facilitating the active regeneration of the oxidized NO_2Lw. Due to the removal of an electron in NO_2Lw, holes are

https://doi.org/10.1021/acsomega.3c06271
ACS Omega 2023, 8, 38748−38765

Table 4. Photovoltaic Performance of TiO_2, ZnO, and Nb_2O_5 Photoanode-based Devices

Sample/Photosensitizer	Dye Adsorption/10^{-7} (mol cm^{-2})	V_{oc} (V)	J_{sc} (mA/cm^2)	FF	R_{tr} (Ω)	R_{rec} (Ω)	τ_e (ms)	η (%)
TiO_2/NO_2Lw	4.96	0.44	0.82	40	236	102,270	63	0.14
ZnO/NO_2Lw	3.06	0.23	0.31	32	1053	47,715	52	0.02
Nb_2O_5/NO_2Lw	0.57	0.24	0.16	42	275	10,111	17	0.01

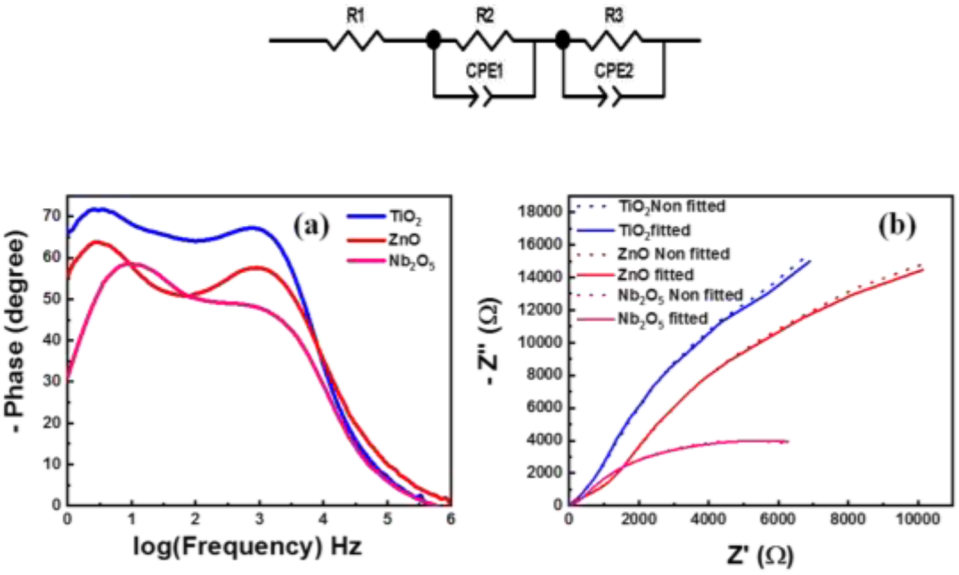

Figure 15. (a) Bode plot and (b) Nyquist plot of TiO_2, ZnO, and Nb_2O_5 photoanode-based devices.

produced at the HOMO level. The holes absorb the electrons from I^-/I_3^- redox couple, which causes I^- to be converted to I_3^- in the electrolyte. The electrons pass through the counter electrode and are transferred to the external circuit. In an oxidation−reduction reaction, the electrons return to the electrolyte.[130−132]

The characteristic curve of NO_2Lw-sensitized TiO_2, ZnO, and Nb_2O_5 photoanode-based DSSCs is shown in Figure 14 as photocurrent density (J_{sc}) versus photovoltage (V). The DSSCs were irradiated with 100 mW cm^{-2} light intensity during the photovoltaic analyses; a polyiodide solution was employed as an electrolyte. The photovoltaics characteristic for TiO_2, ZnO, and Nb_2O_5 photoanodes, including open circuit voltage (V_{oc}), short-circuit photocurrent density (J_{sc}), fill factor (FF), and efficiency (η), were computed and summarized in Table 4.

It was found that TiO_2 has a higher J_{sc} value (J_{sc} = 0.82 mA/cm^2) than ZnO and Nb_2O_5-based photoanodes. ZnO and Nb_2O_5 have J_{sc} values of 0.31 and 0.16 mA/cm^2, respectively. On the other hand, the TiO_2, ZnO, and Nb_2O_5 photoanodes had corresponding V_{oc} values of 0.44, 0.23, and 0.24 V, respectively. TiO_2, ZnO, and Nb_2O_5 photoanodes have FF values of 40, 32, and 42, respectively, and their corresponding power conversion efficiency (PEC) η values are 0.14, 0.02, and 0.01%, respectively. Compared to the ZnO and Nb_2O_5 photoanodes, the TiO_2 photoanode-based DSSC performed better in photovoltaic efficiency. This is because the TiO_2 photoanode, compared to ZnO and Nb_2O_5 photoanodes, has a significantly more considerable photosensitizer loading amount.

The photosensitizer loading amounts of NO_2Lw are calculated and summarized in Table 4 for TiO_2, ZnO, and Nb_2O_5 photoanodes. In addition, compared to ZnO and Nb_2O_5 photoanodes, computed J_{sc} and V_{oc} values for the TiO_2 photoelectrode are greater. Finally, a power conversion efficiency (PCE) of 0.14% was shown by the TiO_2 photoanode.

3.11. Electrochemical Impedance Spectroscopy (EIS) Analysis. EIS measurement was done at a forward bias of open-circuit voltage under dark illumination conditions in the 1 MHz to 0.1 Hz frequency range to explain the electron transportation resistance and charge recombination resistance at different interfaces and determine the effective electron lifetime of the device.

Figure 15a displays the Bode plot with signature frequency peak corresponding to interfacial electron recombination toward the low-frequency region for the TiO_2 in comparison to ZnO and Nb_2O_5 photoanode-based DSSCs, indicating that the TiO_2 has a greater electron lifetime than ZnO and Nb_2O_5 photoanode-based DSSCs. The average electron lifetime (τ_{eff}) of TiO_2, ZnO, and Nb_2O_5 photoanode-based devices can be calculated using the equation[133]

$$\tau_{eff} = \frac{1}{2\pi f_{max}} \quad (2)$$

Table 4 provides a summary of the values. The average electron lifetime for TiO_2 (63 ms) photoanode-based devices was higher in comparison to those for ZnO (52 ms) and Nb_2O_5 (17 ms) photoanode-based DSSCs. This indicates that as compared to ZnO and Nb_2O_5 photoanodes, there is reduced electron recombination at the TiO_2 photoanode/electrolyte interface-based DSSCs.

Figure 15b displays the Nyquist plot of TiO_2, ZnO, and Nb_2O_5 photoanodes-based DSSCs. The electrochemical parameters of all three devices were calculated using Z View fitted software by fitting the measured EIS entities. Table 4 displays the corresponding values. In Figure 15b, the first semicircle depicts the interface between the counter electrode

https://doi.org/10.1021/acsomega.3c06271
ACS Omega 2023, 8, 38748−38765

and an electrolyte, influencing the R_2 (R_{tr}) electron transport resistance. At TiO_2/ZnO/Nb_2O_5/NO_2Lw/electrolyte, the charge recombination resistance of electrons was shown by R_3 (R_{rec}).

In the current study, two semicircles in the EIS curves of the TiO_2, ZnO, and Nb_2O_5-based photoanode are merged. This is because the electron recombination resistance at the TiO_2/ZnO/Nb_2O_5/NO_2Lw/electrolyte process is significantly greater than the other resistance at the counter electrode and electrolyte interface (electron transport resistance, R_{tr}). The smaller semicircle associated with the resistance at the interface between the counter electrode and electrolyte may thus be challenging to detect.

The charge recombination resistance (R_{rec}) is seen to increase in the order Nb_2O_5 < ZnO < TiO_2. Greater R_{rec} in dark illumination is correlated with a lower recombination rate.[134,135] Compared to ZnO and Nb_2O_5 photoanode-based DSSCs, the R_{rec} is greater in TiO_2 photoanode-based DSSCs, indicating a lower recombination rate at the TiO_2 photoanode/electrolyte interface. Thus the optimum values of R_{rec} led to the highest current density and open circuit voltage for TiO_2 compared to ZnO and Nb_2O_5 photoanode-based DSSCs.

4. CONCLUSIONS

In the fabrication and development of DSSCs, the performance of three distinct mesoporous semiconducting oxides, TiO_2, ZnO, and Nb_2O_5, as photoanode materials has been compared. The utilization of NO_2Lw as a photosensitizer for DSSCs is shown for the first time in this study. We looked into photovoltaic parameters such as the V_{OC}, J_{SC}, and power conversion efficiency (PEC). Due to their higher photosensitizer loading amount, greater electron lifetime, and reduced electron recombination rate, the fabricated DSSCs function better with the TiO_2 photoanode than with ZnO and Nb_2O_5 photoanodes. The outcomes suggest a role for injecting electrons from higher excited-state energy (LUMO) levels of NO_2Lw into the conduction band (CB) of the photoanode material, to which the NO_2Lw is chemically bonded.

AUTHOR INFORMATION

Corresponding Author

Sunita Salunke-Gawali − *Department of Chemistry, Savitribai Phule Pune University, Pune 411007, India;* orcid.org/0000-0002-4460-3992; Email: sunita.salunke@unipune.ac.in

Authors

Niyamat I. Beedri − *Department of Chemistry, Savitribai Phule Pune University, Pune 411007, India;* orcid.org/0000-0002-8357-0257

Gaurav Dani − *Department of Chemistry, Savitribai Phule Pune University, Pune 411007, India*

Manisha Gaikwad − *Department of Chemistry, Savitribai Phule Pune University, Pune 411007, India*

Habib M. Pathan − *Advanced Physics Laboratory, Department of Physics, Savitribai Phule Pune University, Pune 411007, India*

Complete contact information is available at: https://pubs.acs.org/10.1021/acsomega.3c06271

Notes

The authors declare no competing financial interest.

ACKNOWLEDGMENTS

Niyamat Beedri is grateful to Savitribai Phule Pune University, Post-Doctoral Fellowship (SPPU-PDF) program (Grant No. SPPU-PDF/ST/PH/2021/0003).

REFERENCES

(1) Sonu; Rani, G. M.; Pathania, D.; Abhimanyu; Umapathi, R.; Rustagi, S.; Huh, Y. S.; Gupta, V. K.; Kaushik, A.; Chaudhary, V. Agro-Waste to Sustainable Energy: A Green Strategy of Converting Agricultural Waste to Nano-Enabled Energy Applications. *Science of The Total Environment* **2023**, *875*, 162667.

(2) Jie, H.; Khan, I.; Alharthi, M.; Zafar, M. W.; Saeed, A. Sustainable Energy Policy, Socio-Economic Development, and Ecological Footprint: The Economic Significance of Natural Resources, Population Growth, and Industrial Development. *Utilities Policy* **2023**, *81*, 101490.

(3) Fan, Q.; Abbas, J.; Zhong, Y.; Pawar, P. S.; Adam, N. A.; Alarif, G. B. Role of Organizational and Environmental Factors in Firm Green Innovation and Sustainable Development: Moderating Role of Knowledge Absorptive Capacity. *Journal of Cleaner Production* **2023**, *411*, 137262.

(4) Ni, Z.; Yang, J.; Razzaq, A. How Do Natural Resources, Digitalization, and Institutional Governance Contribute to Ecological Sustainability through Load Capacity Factors in Highly Resource-Consuming Economies? *Resources Policy* **2022**, *79*, 103068.

(5) Dey, S.; Sreenivasulu, A.; Veerendra, G. T. N.; Rao, K. V.; Babu, P. S. S. A. Renewable Energy Present Status and Future Potentials in India: An Overview. *Innovation and Green Development* **2022**, *1* (1), 100006.

(6) Santika, W. G.; Anisuzzaman, M.; Bahri, P. A.; Shafiullah, G. M.; Rupf, G. V.; Urmee, T. From Goals to Joules: A Quantitative Approach of Interlinkages between Energy and the Sustainable Development Goals. *Energy Research & Social Science* **2019**, *50*, 201−214.

(7) Kabeyi, M. J. B.; Olanrewaju, O. A. Sustainable Energy Transition for Renewable and Low Carbon Grid Electricity Generation and Supply. *Front. Energy Res.* **2022**, *9*, 743114.

(8) Cai, K.; Wu, H.; Hua, T.; Liao, C.; Tang, H.; Wang, L.; Cao, D. Molecular Engineering of the Fused Azacycle Donors in the D-A-π-A Metal-Free Organic Dyes for Efficient Dye-Sensitized Solar Cells. *Dyes Pigm.* **2022**, *197*, 109922.

(9) Huang, H.; Yan, Z. Present Situation and Future Prospect of Hydropower in China. *Renewable and Sustainable Energy Reviews* **2009**, *13* (6−7), 1652−1656.

(10) Bejarano, M. D.; Sordo-Ward, A.; Gabriel-Martin, I.; Garrote, L. Tradeoff between Economic and Environmental Costs and Benefits of Hydropower Production at Run-of-River-Diversion Schemes under Different Environmental Flows Scenarios. *Journal of Hydrology* **2019**, *572*, 790−804.

(11) Smakhtin, V. U. Low Flow Hydrology: A Review. *Journal of Hydrology* **2001**, *240* (3−4), 147−186.

(12) Holechek, J. L.; Geli, H. M. E.; Sawalhah, M. N.; Valdez, R. A Global Assessment: Can Renewable Energy Replace Fossil Fuels by 2050? *Sustainability* **2022**, *14* (8), 4792.

(13) Sen, A.; Putra, M. H.; Biswas, A. K.; Behera, A. K.; Groβ, A. Insight on the Choice of Sensitizers/Dyes for Dye Sensitized Solar Cells: A Review. *Dyes Pigm.* **2023**, *213*, 111087.

(14) Zhao, Q.; Lai, C.; Zhang, H.; Hu, Z. A Broad-Spectrum Solar Energy Power System by Hybridizing Stirling-like Thermocapacitive Cycles to Dye-Sensitized Solar Cells. *Renewable Energy* **2023**, *205*, 94−104.

(15) Sun, L.; Chen, Y.; Sun, M.; Zheng, Y. Organic Solar Cells: Physical Principle and Recent Advances. *Chemistry An Asian Journal* **2023**, *18* (5), e202300006.

(16) Vodapally, S. N.; Ali, M. H. A Comprehensive Review of Solar Photovoltaic (PV) Technologies, Architecture, and Its Applications to Improved Efficiency. *Energies* **2023**, *16* (1), 319.

(17) Chen, L. X. Organic Solar Cells: Recent Progress and Challenges. *ACS Energy Lett.* **2019**, *4* (10), 2537−2539.
(18) Sharma, K.; Sharma, V.; Sharma, S. S. Dye-Sensitized Solar Cells: Fundamentals and Current Status. *Nanoscale Res. Lett.* **2018**, *13* (1), 381.
(19) Hong, S.; Lee, J. Recent Advances and Challenges toward Efficient Perovskite/Organic Integrated Solar Cells. *Energies* **2023**, *16* (1), 266.
(20) Molina, D.; Follana-Berna, J.; Sastre-Santos, A. Phthalocyanines, Porphyrins and Other Porphyrinoids as Components of Perovskite Solar Cells. *J. Mater. Chem. C* **2023**, *11* (24), 7885.
(21) Basit, M. A.; Aanish Ali, M.; Masroor, Z.; Tariq, Z.; Bang, J. H. Quantum Dot-Sensitized Solar Cells: A Review on Interfacial Engineering Strategies for Boosting Efficiency. *Journal of Industrial and Engineering Chemistry* **2023**, *120*, 1−26.
(22) Kaur, N.; Singh, D. P.; Mahajan, A. Plasmonic Engineering of TiO2 Photoanodes for Dye-Sensitized Solar Cells: A Review. *J. Electron. Mater.* **2022**, *51* (8), 4188−4206.
(23) Shao, J.-Y.; Li, D.; Shi, J.; Ma, C.; Wang, Y.; Liu, X.; Jiang, X.; Hao, M.; Zhang, L.; Liu, C.; Jiang, Y.; Wang, Z.; Zhong, Y.-W.; Liu, S. F.; Mai, Y.; Liu, Y.; Zhao, Y.; Ning, Z.; Wang, L.; Xu, B.; Meng, L.; Bian, Z.; Ge, Z.; Zhan, X.; You, J.; Li, Y.; Meng, Q. Recent Progress in Perovskite Solar Cells: Material Science. *Sci. China Chem.* **2023**, *66* (1), 10−64.
(24) Zhang, Q.; Li, F.; Xu, L. Application of Polyoxometalates in Third-Generation Solar Cells. *Polyoxometalates* **2023**, *2* (1), 9140018.
(25) Xu, B.; Wang, L.; Li, X.; Yang, X.; Lü, W. A Facile Method to Fabricate Transparent TiO_2 Photoanodes for Quantum Dot-Sensitized Solar Cells. *Ionics* **2022**, *28* (6), 3049−3056.
(26) Pawar, S.; Lokhande, P. E.; Kaur, J.; Dubey, R. S.; Pathan, H. M. Monochromatic Photochemical Deposition and Characterization of ZnSe Thin Films. *ES Energy Environ.* **2022**, *17*, 86−93.
(27) Kishore Kumar, D.; Kříž, J.; Bennett, N.; Chen, B.; Upadhayaya, H.; Reddy, K. R.; Sadhu, V. Functionalized Metal Oxide Nanoparticles for Efficient Dye-Sensitized Solar Cells (DSSCs): A Review. *Materials Science for Energy Technologies* **2020**, *3*, 472−481.
(28) Kokkonen, M.; Talebi, P.; Zhou, J.; Asgari, S.; Soomro, S. A.; Elsehrawy, F.; Halme, J.; Ahmad, S.; Hagfeldt, A.; Hashmi, S. G. Advanced Research Trends in Dye-Sensitized Solar Cells. *J. Mater. Chem. A* **2021**, *9* (17), 10527−10545.
(29) Maka, A. O. M.; Alabid, J. M. Solar Energy Technology and Its Roles in Sustainable Development. *Clean Energy* **2022**, *6* (3), 476−483.
(30) Bandara, T. M. W. J.; Hansadi, J. M. C.; Bella, F. A Review of Textile Dye-Sensitized Solar Cells for Wearable Electronics. *Ionics* **2022**, *28* (6), 2563−2583.
(31) Mariotti, N.; Bonomo, M.; Fagiolari, L.; Barbero, N.; Gerbaldi, C.; Bella, F.; Barolo, C. Recent Advances in Eco-Friendly and Cost-Effective Materials towards Sustainable Dye-Sensitized Solar Cells. *Green Chem.* **2020**, *22* (21), 7168−7218.
(32) Richhariya, G.; Meikap, B. C.; Kumar, A. Review on Fabrication Methodologies and Its Impacts on Performance of Dye-Sensitized Solar Cells. *Environ. Sci. Pollut Res.* **2022**, *29* (11), 15233−15251.
(33) Bhand, S.; Salunke-Gawali, S. Amphiphilic Photosensitizers in Dye Sensitized Solar Cells. *Inorg. Chim. Acta* **2019**, *495*, 118955.
(34) Pawar, K. S.; Baviskar, P. K.; Inamuddin; Nadaf, A. B.; Salunke-Gawali, S.; Pathan, H. M. Layer-by-Layer Deposition of TiO2-ZrO2 Electrode Sensitized with Pandan Leaves: Natural Dye-Sensitized Solar Cell. *Mater. Renew Sustain Energy* **2019**, *8* (2), 12.
(35) Dhonde, M.; Sahu, K.; Das, M.; Yadav, A.; Ghosh, P.; Murty, V. V. S. Review—Recent Advancements in Dye-Sensitized Solar Cells; From Photoelectrode to Counter Electrode. *J. Electrochem. Soc.* **2022**, *169* (6), 066507.
(36) Beedri, N. I.; Baviskar, P. K.; Bhalekar, V. P.; Jagtap, C. V.; Asiri, A. M.; Jadkar, S. R.; Pathan, H. M. N3-Sensitized TiO_2/Nb_2O_5: A Novel Bilayer Structure for Dye-Sensitized Solar-Cell Application. *Phys. Status Solidi A* **2018**, *215* (18), 1800236.
(37) Beedri, N. I.; Baviskar, P. K.; Mahadik, M.; Jadkar, S. R.; Jang, J. S.; Pathan, H. M. Efficiency Enhancement for Cocktail Dye Sensitized Nb_2O_5 Photoanode Towards Dye Sensitized Solar Cell. *Eng. Sci.* **2019**, *8*, 76−82.
(38) O'Regan, B.; Grätzel, M. A Low-Cost, High-Efficiency Solar Cell Based on Dye-Sensitized Colloidal TiO_2 Films. *Nature* **1991**, *353* (6346), 737−740.
(39) Güzel, E.; Medina, D.-P.; Medel, M.; Kandaz, M.; Torres, T.; Rodríguez-Morgade, M. S. A Versatile, Divergent Route for the Synthesis of ABAC Tetraazaporphyrins: Molecularly Engineered, Push-Pull Phthalocyanine-Type Dyes. *J. Mater. Chem. C* **2021**, *9* (33), 10802−10810.
(40) Pashaei, B.; Shahroosvand, H. Molecularly Engineered Ruthenium Polypyridyl Complexes for Using in Dye-Sensitized Solar Cell. *Inorg. Chem. Commun.* **2020**, *112*, 107737.
(41) Chandrasekharam, M.; Rajkumar, G.; Srinivasa Rao, C.; Suresh, T.; Yella Reddy, P.; Yum, J.-H.; Khaja Nazeeruddin, M.; Graetzel, M. A Molecularly Engineered Fluorene-Substituted Ru-Complex for Efficient Mesoscopic Dye-Sensitized Solar Cells. *Adv. Nat. Sci: Nanosci. Nanotechnol.* **2011**, *2* (3), 035016.
(42) Alnakeeb, A.; Fadda, A. A.; Ismail, M. A.; Elmorsy, M. R. Efficient Co-Sensitization of Novel Trimethoxybenzene-Based Dyes with N-719 for Highly Efficient Dye-Sensitized Solar Cells. *Opt. Mater.* **2022**, *128*, 112344.
(43) Sahoo, S. S.; Murmu, M.; Banerjee, P.; Pathan, H. M.; Salunke-Gawali, S. Tailoring Benzo[α]Phenoxazine Moiety for Efficient Photosensitizers in Dye Sensitized Solar Cells *via* the DFT/TD-DFT Method. *New J. Chem.* **2022**, *46* (31), 15155−15167.
(44) Baptayev, B.; Kim, S.-M.; Bolatbek, B.; Lee, S. H.; Balanay, M. P. Effect of π-Spacer Length in Novel Xanthene-Linked L -(D-π-A)2 -Type Dianchoring Dyes for Dye-Sensitized Solar Cells. *ACS Appl. Energy Mater.* **2022**, *5* (6), 6764−6771.
(45) Subalakshmi, K.; Chung, W.; Lee, S. Synergistically Improved Photovoltaic Performances of Dye-Sensitized Solar Cells with Metal-Free Organic Cosensitizer and Hybrid RGO-TiO_2 Photoanode. *Dyes Pigm.* **2023**, *209*, 110892.
(46) Cheng, H.-M.; Hsieh, W.-F. High-Efficiency Metal-Free Organic-Dye-Sensitized Solar Cells with Hierarchical ZnO Photoelectrode. *Energy Environ. Sci.* **2010**, *3* (4), 442.
(47) Luo, J.; Xu, M.; Li, R.; Huang, K.-W.; Jiang, C.; Qi, Q.; Zeng, W.; Zhang, J.; Chi, C.; Wang, P.; Wu, J. *N* -Annulated Perylene as An Efficient Electron Donor for Porphyrin-Based Dyes: Enhanced Light-Harvesting Ability and High-Efficiency Co(II/III)-Based Dye-Sensitized Solar Cells. *J. Am. Chem. Soc.* **2014**, *136* (1), 265−272.
(48) Mathew, S.; Yella, A.; Gao, P.; Humphry-Baker, R.; Curchod, B. F. E.; Ashari-Astani, N.; Tavernelli, I.; Rothlisberger, U.; Nazeeruddin, Md. K.; Grätzel, M. Dye-Sensitized Solar Cells with 13% Efficiency Achieved through the Molecular Engineering of Porphyrin Sensitizers. *Nature Chem.* **2014**, *6* (3), 242−247.
(49) Ito, S.; Miura, H.; Uchida, S.; Takata, M.; Sumioka, K.; Liska, P.; Comte, P.; Péchy, P.; Grätzel, M. High-Conversion-Efficiency Organic Dye-Sensitized Solar Cells with a Novel Indoline Dye. *Chem. Commun.* **2008**, No. 41, 5194.
(50) Ooyama, Y.; Inoue, S.; Asada, R.; Ito, G.; Kushimoto, K.; Komaguchi, K.; Imae, I.; Harima, Y. Dye-Sensitized Solar Cells Based on a Novel Fluorescent Dye with a Pyridine Ring and a Pyridinium Dye with the Pyridinium Ring Forming Strong Interactions with Nanocrystalline TiO2 Films. *Eur. J. Org. Chem.* **2010**, *2010* (1), 92.
(51) Wu, Y.; Zhang, X.; Li, W.; Wang, Z.-S.; Tian, H.; Zhu, W. Hexylthiophene-Featured D-A-π-A Structural Indoline Chromophores for Coadsorbent-Free and Panchromatic Dye-Sensitized Solar Cells. *Adv. Energy Mater.* **2012**, *2* (1), 149−156.
(52) Clifford, J. N.; Martínez-Ferrero, E.; Viterisi, A.; Palomares, E. Sensitizer Molecular Structure-Device Efficiency Relationship in Dye Sensitized Solar Cells. *Chem. Soc. Rev.* **2011**, *40* (3), 1635−1646.
(53) Hagfeldt, A.; Boschloo, G.; Sun, L.; Kloo, L.; Pettersson, H. Dye-Sensitized Solar Cells. *Chem. Rev.* **2010**, *110* (11), 6595−6663.
(54) Pfattner, R.; Pavlica, E.; Jaggi, M.; Liu, S.-X.; Decurtins, S.; Bratina, G.; Veciana, J.; Mas-Torrent, M.; Rovira, C. Photo-Induced

https://doi.org/10.1021/acsomega.3c06271
ACS Omega 2023, 8, 38748−38765

Intramolecular Charge Transfer in an Ambipolar Field-Effect Transistor Based on a π-Conjugated Donor-Acceptor Dyad. *J. Mater. Chem. C* **2013**, *1* (25), 3985.
(55) Schoden, F.; Schnatmann, A. K.; Blachowicz, T.; Manz-Schumacher, H.; Schwenzfeier-Hellkamp, E. Circular Design Principles Applied on Dye-Sensitized Solar Cells. *Sustainability* **2022**, *14* (22), 15280.
(56) Pu, H.; Fang, T.; Wu, Z.; Sun, D.-W. Advancements in Recyclable Photocatalytic Semiconductor Substrates for SERS Detection in Food Safety Applications. *Trends in Food Science & Technology* **2023**, *138*, 697−707.
(57) Khanmohammadi Chenab, K.; Sohrabi, B.; Zamani Meymian, M. R.; Mousavi, S. V. Naphthoquinone Derivative-Based Dye for Dye-Sensitized Solar Cells: Experimental and Computational Aspects. *Mater. Res. Express* **2019**, *6* (8), 085537.
(58) Khanmohammadi, K.; Sohrabi, B.; Zamani Meymian, M. R. Effect of Electron-Donating and -Withdrawing Substitutions in Naphthoquinone Sensitizers: The Structure Engineering of Dyes for DSSCs. *J. Mol. Struct.* **2018**, *1167*, 274−279.
(59) Mahadik, S. A.; Salunke-Gawali, S. 2-Chloro-(n-Alkylamino)-Pyridine-1,4-Naphthoquinones as Photosensitizers in TiO_2 and ZnO-Based DSSCs. *J. Mater. Sci: Mater. Electron* **2023**, *34* (22), 1609.
(60) Shinde, D.; Tambade, P.; Pathan, H.; Gadave, K. Experimental and Theoretical Study of 1, 4-Naphthoquinone Based Dye in Dye-Sensitized Solar Cells Using ZnO Photoanode. *Materials Science-Poland* **2017**, *35* (4), 746−754.
(61) Mahadik, S. A.; Pathan, H. M.; Salunke-Gawali, S.; Butcher, R. J. Titania Nanorods Embedded with 2-Bromo-3-(Methylamino)-Naphthalene-1,4-Dione for Dye-Sensitized Solar Cells. *ACS Omega* **2022**, *7* (40), 35595−35609.
(62) Bhand, S.; Chadar, D.; Pawar, K.; Naushad, M.; Pathan, H.; Salunke-Gawali, S. Benzo[α]Phenothiazine Sensitized ZrO_2 Based Dye Sensitized Solar Cell. *J. Mater. Sci: Mater. Electron* **2018**, *29* (2), 1034−1041.
(63) Khadtare, S. S.; Ware, A. P.; Salunke-Gawali, S.; Jadkar, S. R.; Pingale, S. S.; Pathan, H. M. Dye Sensitized Solar Cell with Lawsone Dye Using a ZnO Photoanode: Experimental and TD-DFT Study. *RSC Adv.* **2015**, *5* (23), 17647−17652.
(64) S., S.; Pesala, B. Performance Enhancement of Betanin Solar Cells Co-Sensitized with Indigo and Lawsone: A Comparative Study. *ACS Omega* **2019**, *4* (19), 18023−18034.
(65) Beedri, N. I.; Mokashi, V. B.; Mahadik, S. A.; Pathan, H. M.; Salunke-Gawali, S. Naphthoquinoneoxime-Sensitized Titanium Dioxide Photoanodes: Photoelectrochemical Properties. *ACS Omega* **2022**, *7* (45), 41519−41530.
(66) Mahadik, S. A.; Pathan, H. M.; Salunke-Gawali, S.; Butcher, R. J. Aminonaphthoquinones as Photosensitizers for Mesoporous ZnO Based Dye-Sensitized Solar Cells. *J. Alloys Compd.* **2020**, *845*, 156279.
(67) Sahoo, S. S.; Chadar, D.; Murmu, M.; Banerjee, P.; Salunke-Gawali, S.; Butcher, R. J. Evaluation of Physicochemical Properties of Provitamin K3 Derived Benzo[α]Phenoxazine as a Photosensitizer. *Eng. Sci.* **2021**, *14*, 94−108.
(68) Mahadik, S. A.; Patil, A.; Pathan, H. M.; Salunke-Gawali, S.; Butcher, R. J. Thionaphthoquinones as Photosensitizers for TiO_2 Nanorods and ZnO Nanograin Based Dye-Sensitized Solar Cells: Effect of Nanostructures on Charge Transport and Photovoltaic Performance. *Eng. Sci.* **2020**, *14*, 46−58.
(69) Lakshmi, R.; Krishnakumar, G.; Joseph, L. K.; Sreelatha, K. S.; Jinchu, I. Lawsone Dye Complex: An Efficient Sensitizer for Dye Sensitized Solar Cell. In *2016 International Conference on Electrical, Electronics, and Optimization Techniques (ICEEOT)*; IEEE: Chennai, India, 2016; pp 4636−4638.
(70) Bonomo, M.; Sabuzi, F.; Di Carlo, A.; Conte, V.; Dini, D.; Galloni, P. KuQuinones as Sensitizers for NiO Based P-Type Dye-Sensitized Solar Cells. *New J. Chem.* **2017**, *41* (7), 2769−2779.
(71) Zhang, L.; Cole, J. M.; Waddell, P. G.; Low, K. S.; Liu, X. Relating Electron Donor and Carboxylic Acid Anchoring Substitution Effects in Azo Dyes to Dye-Sensitized Solar Cell Performance. *ACS Sustainable Chem. Eng.* **2013**, *1* (11), 1440−1452.
(72) Chen, Y.-S.; Li, C.; Zeng, Z.-H.; Wang, W.-B.; Wang, X.-S.; Zhang, B.-W. Efficient Electron Injection Due to a Special Adsorbing Group's Combination of Carboxyl and Hydroxyl: Dye-Sensitized Solar Cells Based on New Hemicyanine Dyes. *J. Mater. Chem.* **2005**, *15* (16), 1654−1661.
(73) Rajendra Prasad, M. B.; Pathan, H. M. Room Temperature Synthesis of Rutile Titania Nanoparticles: A Thermodynamic Perspective. *Eur. Phys. J. D* **2014**, *68* (2), 25.
(74) Prasad M B, R.; Pathan, H. M. Effect of Photoanode Surface Coverage by a Sensitizer on the Photovoltaic Performance of Titania Based CdS Quantum Dot Sensitized Solar Cells. *Nanotechnology* **2016**, *27* (14), 145402.
(75) Rane, S. Y.; Khan, E. M.; Khursheed, Ah.; Salunke-Gawali, S. Ligand Induced Stereoisomers Revealed in Copper(II) Complex of Nitrolawsone Oxime: EPR and Electronic Spectral Studies. *Synthesis and Reactivity in Inorganic, Metal-Organic, and Nano-Metal Chemistry* **2005**, *35* (5), 343−353.
(76) Zhang, Q. Effects of Calcination on the Photocatalytic Properties of Nanosized TiO_2 Powders Prepared by $TiCl_4$ Hydrolysis. *Applied Catalysis B: Environmental* **2000**, *26* (3), 207−215.
(77) A R Sayyed, S. A.; Beedri, N. I.; Kadam, V. S.; Pathan, H. M. Rose Bengal-Sensitized Nanocrystalline Ceria Photoanode for Dye-Sensitized Solar Cell Application. *Bull. Mater. Sci.* **2016**, *39* (6), 1381−1387.
(78) Sayyed, S. A. A. R.; Beedri, N. I.; Pathan, H. M. Spinach Extract and Eosin-Y Co-Sensitized Ceria Photoanode for Dye Sensitized Solar Cell Application: Effect of Dye Adsorption Time. *J. Mater. Sci: Mater. Electron* **2017**, *28* (6), 5075−5081.
(79) Mani, J.; Sakeek, H.; Habouti, S.; Dietze, M.; Es-Souni, M. Macro-Meso-Porous TiO_2, ZnO and ZnO-TiO_2 -Composite Thick Films. Properties and Application to Photocatalysis. *Catal. Sci. Technol.* **2012**, *2* (2), 379−385.
(80) Lin, J.; Yuan, Y.; Su, Q.; Pan, A.; Dinesh, S.; Peng, C.; Cao, G.; Liang, S. Facile Synthesis of Nb_2O_5/Carbon Nanocomposites as Advanced Anode Materials for Lithium-Ion Batteries. *Electrochim. Acta* **2018**, *292*, 63−71.
(81) Luo, H.; Song, W.; Hoertz, P. G.; Hanson, K.; Ghosh, R.; Rangan, S.; Brennaman, M. K.; Concepcion, J. J.; Binstead, R. A.; Bartynski, R. A.; Lopez, R.; Meyer, T. J. A Sensitized Nb_2O_5 Photoanode for Hydrogen Production in a Dye-Sensitized Photoelectrosynthesis Cell. *Chem. Mater.* **2013**, *25* (2), 122−131.
(82) Inamdar, Y.; Beedri, N.; Kodam, K.; Shaikh, A.; Pathan, H. Aggregation of ZnO Nanocrystallites Using Polyol Process for Dye (Reactive Red) Sensitized Solar Cell: Aggregation of ZnO Nanocrystallites Using Polyol. *Macromol. Symp.* **2015**, *347* (1), 52−57.
(83) Kim, J. S.; Shin, S. S.; Han, H. S.; Shin, S.; Suk, J. H.; Kang, K.; Hong, K. S.; Cho, I. S. Facile Preparation of TiO_2 Nanobranch/Nanoparticle Hybrid Architecture with Enhanced Light Harvesting Properties for Dye-Sensitized Solar Cells. *J. Nanomater.* **2015**, *2015*, 1−9.
(84) Jo, M.; Cho, J.; Wang, X.; Jin, E.; Jeong, S.; Kang, D.-W. Improving of the Photovoltaic Characteristics of Dye-Sensitized Solar Cells Using a Photoelectrode with Electrospun Porous TiO_2 Nanofibers. *Nanomaterials* **2019**, *9* (1), 95.
(85) Inamdar, Y. A.; Beedri, N. I.; Shaikh, A. V.; Kodam, K. M.; Pathan, H. M. ZnO Photoelectrode for Textile Dye (Reactive Blue 59) Sensitized Solar Cell. *Adv. Sci. Lett.* **2014**, *20* (5), 1155−1158.
(86) Sayyed, S. A. A. R.; Beedri, N. I.; Bhujbal, P. K.; Shaikh, S. F.; Pathan, H. M. Eosin-Y Sensitized Bi-Layered ZnO Nanoflower-CeO_2 Photoanode for Dye-Sensitized Solar Cells Application. *ES Mater. Manuf.* **2020**, *10* (2), 45−51.
(87) Beedri, N. I.; Sayyed, S. A. A. R.; Jadkar, S. R.; Pathan, H. M. Rose Bengal Sensitized Niobium Pentaoxide Photoanode for Dye Sensitized Solar Cell Application; In *AIP Conference Proceedings*, 2017, Vol. *1832* (1), p 040022.
(88) Le Viet, A.; Jose, R.; Reddy, M. V.; Chowdari, B. V. R.; Ramakrishna, S. Nb_2O_5 Photoelectrodes for Dye-Sensitized Solar Cells: Choice of the Polymorph. *J. Phys. Chem. C* **2010**, *114* (49), 21795−21800.

https://doi.org/10.1021/acsomega.3c06271
ACS Omega 2023, 8, 38748−38765

(89) Zhang, H.; Wang, Y.; Yang, D.; Li, Y.; Liu, H.; Liu, P.; Wood, B. J.; Zhao, H. Directly Hydrothermal Growth of Single Crystal $Nb_3O_7(OH)$ Nanorod Film for High Performance Dye-Sensitized Solar Cells. *Adv. Mater.* **2012**, *24* (12), 1598−1603.
(90) Lungu, J.; Socol, G.; Stan, G. E.; Ştefan, N.; Luculescu, C.; Georgescu, A.; Popescu-Pelin, G.; Prodan, G.; Gîrţu, M. A.; Mihăilescu, I. N. Pulsed Laser Fabrication of TiO_2 Buffer Layers for Dye Sensitized Solar Cells. *Nanomaterials* **2019**, *9* (5), 746.
(91) Lokhande, P. E.; Chavan, U. S.; Deokar, S.; Ingale, M.; Bhosale, S.; Kale, S.; Kamte, A. Surfactant Free Chemically Deposited Wheat Spike-like Nanostructure on Cu Foam for Supercapacitor Applications. *Materials Today: Proceedings* **2019**, *18*, 979−985.
(92) Lokhande, P. E.; Kadam, V.; Jagatap, C.; Chavan, U. S.; R, U.; Pathan, H. M Hierarchical Ultrathin Nanosheet of $Ni(OH)_2$/RGO Composite Chemically Deposited on Ni Foam for NOx Gas Sensors. *ES Mater. Manuf.* **2022**, *17*, 53−56.
(93) Khadtare, S. S.; Jadkar, S. R.; Salunke-Gawali, S.; Pathan, H. M. Lawsone Sensitized ZnO Photoelectrodes for Dye Sensitized Solar Cells. *JNanoR* **2013**, *24*, 140−145.
(94) Usgodaarachchi, L.; Thambiliyagodage, C.; Wijesekera, R.; Vigneswaran, S.; Kandanapitiye, M. Fabrication of TiO_2 Spheres and a Visible Light Active α-Fe_2O_3 /TiO_2 -Rutile/TiO_2 -Anatase Heterogeneous Photocatalyst from Natural Ilmenite. *ACS Omega* **2022**, *7* (31), 27617−27637.
(95) Essien, E. R.; Atasie, V. N.; Nwude, D. O.; Adekolurejo, E.; Owoeye, F. T. Characterisation of ZnO Nanoparticles Prepared Using Aqueous Leaf Extracts of Chromolaena Odorata (L.) and Manihot Esculenta (Crantz). *S. Afr. J. Sci.* **2022**, *118* (1/2), 11225.
(96) Ge, J.; Wang, F.; Xu, Z.; Shen, X.; Gao, C.; Wang, D.; Hu, G.; Gu, J.; Tang, T.; Wei, J. Influences of Niobium Pentoxide on Roughness, Hydrophilicity, Surface Energy and Protein Absorption, and Cellular Responses to PEEK Based Composites for Orthopedic Applications. *J. Mater. Chem. B* **2020**, *8* (13), 2618−2626.
(97) Alwin, S.; Shajan, X. S.; Karuppasamy, K.; Warrier, K. G. K. Microwave Assisted Synthesis of High Surface Area TiO_2 Aerogels: A Competent Photoanode Material for Quasi-Solid Dye-Sensitized Solar Cells. *Mater. Chem. Phys.* **2017**, *196*, 37−44.
(98) Miao, L.; Jin, P.; Kaneko, K.; Terai, A.; Nabatova-Gabain, N.; Tanemura, S. Preparation and Characterization of Polycrystalline Anatase and Rutile TiO_2 Thin Films by Rf Magnetron Sputtering. *Appl. Surf. Sci.* **2003**, *212*−*213*, 255−263.
(99) Hosseinpour, M.; Mirzaee, O.; Alamdari, S.; Menéndez, J. L.; Abdoos, H. Novel PWO/ ZnO Heterostructured Nanocomposites: Synthesis, Characterization, and Photocatalytic Performance. *Journal of Environmental Management* **2023**, *345*, 118586.
(100) Yang, L.; Wei, Y.; Song, Y.; Peng, Y.; Yang, Y.; Huang, Z. Surface-Enhanced Raman Scattering from Amorphous Nanoflower-Structural Nb_2O_5 Fabricated by Two-Step Hydrothermal Technology. *Materials & Design* **2020**, *193*, 108808.
(101) Xu, Y.; Li, Z.; Zhang, F.; Zhuang, X.; Zeng, Z.; Wei, J. New Nitrogen-Rich Azo-Bridged Porphyrin-Conjugated Microporous Networks for High Performance of Gas Capture and Storage. *RSC Adv.* **2016**, *6* (36), 30048−30055.
(102) Madurai Ramakrishnan, V.; Pitchaiya, S.; Muthukumarasamy, N.; Kvamme, K.; Rajesh, G.; Agilan, S.; Pugazhendhi, A.; Velauthapillai, D. Performance of TiO_2 Nanoparticles Synthesized by Microwave and Solvothermal Methods as Photoanode in Dye-Sensitized Solar Cells (DSSC). *Int. J. Hydrogen Energy* **2020**, *45* (51), 27036−27046.
(103) Liu, X.; Mao, Z.; Liu, J.; Meng, F.; Shi, X.; Xue, X.; Zhao, B. Probing the Open-Circuit Voltage Improvement of DSSC via Raman Spectroscopy: *In Situ* Dynamic Tracking Photoanode/Electrolyte Interfaces. *ACS Appl. Energy Mater.* **2022**, *5* (7), 8391−8399.
(104) Lee, K. E.; Gomez, M. A.; Regier, T.; Hu, Y.; Demopoulos, G. P. Further Understanding of the Electronic Interactions between N719 Sensitizer and Anatase TiO_2 Films: A Combined X-Ray Absorption and X-Ray Photoelectron Spectroscopic Study. *J. Phys. Chem. C* **2011**, *115* (13), 5692−5707.
(105) Xu, L.; Wei, B.; Liu, W.; Zhang, H.; Su, C.; Che, J. Flower-like ZnO-Ag_2O Composites: Precipitation Synthesis and Photocatalytic Activity. *Nanoscale Res. Lett.* **2013**, *8* (1), 536.
(106) Pandey, S. K.; Pandey, S. K.; Mukherjee, C.; Mishra, P.; Gupta, M.; Barman, S. R.; D'Souza, S. W.; Mukherjee, S. Effect of Growth Temperature on Structural, Electrical and Optical Properties of Dual Ion Beam Sputtered ZnO Thin Films. *J. Mater. Sci: Mater. Electron* **2013**, *24* (7), 2541−2547.
(107) Jing, L. Relationships of Surface Oxygen Vacancies with Photoluminescence and Photocatalytic Performance of ZnO Nanoparticles. *Sci. China Ser. B* **2005**, *48* (1), 25.
(108) Wang, L.; Huang, F.; Zhu, G.; Dai, Z. Nb_2O_5 Nanocrystals Decorated Graphene Composites as Anode Materials for High-Performance Dual-Ion Batteries. *Nano Res.* **2023**, 1.
(109) Falk, G.; Borlaf, M.; López-Muñoz, M. J.; Fariñas, J. C.; Rodrigues Neto, J. B.; Moreno, R. Microwave-Assisted Synthesis of Nb2O5 for Photocatalytic Application of Nanopowders and Thin Films. *J. Mater. Res.* **2017**, *32* (17), 3271−3278.
(110) Cho, F.-H.; Kuo, S.-C.; Lai, Y.-H. Surface-Plasmon-Induced Azo Coupling Reaction between Nitro Compounds on Dendritic Silver Monitored by Surface-Enhanced Raman Spectroscopy. *RSC Adv.* **2017**, *7* (17), 10259−10265.
(111) Wang, X.; Wang, Y.; Sui, H.; Zhang, X.; Su, H.; Cheng, W.; Han, X. X.; Zhao, B. Investigation of Charge Transfer in Ag/N719/TiO_2 Interface by Surface-Enhanced Raman Spectroscopy. *J. Phys. Chem. C* **2016**, *120* (24), 13078−13086.
(112) Firtina-Ertis, I.; Kerkez-Kuyumcu, Ö. Synthesis of $NiFe_2O_4$/TiO_2-Ag^+ S-Scheme Photocatalysts by a Novel Complex-Assisted Vapor Thermal Method for Photocatalytic Hydrogen Production. *J. Photochem. Photobiol., A* **2022**, *432*, 114106.
(113) Bhujbal, P. K.; Pathan, H. M.; Chaure, N. B. Deposition of Amorphous and Crystalline Al Doped ZnO Thin Films by RF Magnetron Sputtering and Their Comparative Properties. *ES Energy Environ.* **2019**, *4*, 15−18.
(114) Bhujbal, P. K.; Pathan, H. M.; Chaure, N. B. Temperature Dependent Studies on Radio Frequency Sputtered Al Doped ZnO Thin Film. *Eng. Sci.* **2020**, *10*, 58−67.
(115) Wang, M.; Wang, H.; Ren, Y.; Wang, C.; Weng, Z.; Yue, B.; He, H. Construction of G-C_3N_4-MNb_2O_5 Composites with Enhanced Visible Light Photocatalytic Activity. *Nanomaterials* **2018**, *8* (6), 427.
(116) Xiang, Q.; Lv, K.; Yu, J. Pivotal Role of Fluorine in Enhanced Photocatalytic Activity of Anatase TiO_2 Nanosheets with Dominant (001) Facets for the Photocatalytic Degradation of Acetone in Air. *Applied Catalysis B: Environmental* **2010**, *96* (3−4), 557−564.
(117) Vinaayak, S. B.; Balasubramani, V.; Shkir, M.; Manthrammel, M. A.; Sreedevi, G. Enhancing the Performance of TiO_2 Based N-DSSC Using Dye Extracted from Cladophora Columbiana, Ludwigia Repens and Mixed Sensitizer. *Opt. Mater.* **2022**, *133*, 112968.
(118) Liu, B.-Q.; Zhao, X.-P.; Luo, W. The Synergistic Effect of Two Photosynthetic Pigments in Dye-Sensitized Mesoporous TiO2 Solar Cells. *Dyes Pigm.* **2008**, *76* (2), 327−331.
(119) Vandewal, K.; Benduhn, J.; Nikolis, V. C. How to Determine Optical Gaps and Voltage Losses in Organic Photovoltaic Materials. *Sustainable Energy Fuels* **2018**, *2* (3), 538−544.
(120) Sahoo, S. S.; Salunke-Gawali, S.; Kadam, V. S.; Pathan, H. M. Canna Lily Red, and Yellow Flower Extracts: A New Power Source to Produce Photovoltage through Dye-Sensitized Solar Cells. *Energy Fuels* **2020**, *34* (8), 9674−9682.
(121) Ketterer, B.; Heiss, M.; Livrozet, M. J.; Rudolph, A.; Reiger, E.; Fontcuberta i Morral, A. Determination of the Band Gap and the Split-off Band in Wurtzite GaAs Using Raman and Photoluminescence Excitation Spectroscopy. *Phys. Rev. B* **2011**, *83* (12), 125307.
(122) Adeniyi, A. A.; Ngake, T. L.; Conradie, J. Cyclic Voltammetric Study of 2-Hydroxybenzophenone (HBP) Derivatives and the Correspondent Change in the Orbital Energy Levels in Different Solvents. *Electroanalysis* **2020**, *32* (12), 2659−2668.
(123) Cardona, C. M.; Li, W.; Kaifer, A. E.; Stockdale, D.; Bazan, G. C. Electrochemical Considerations for Determining Absolute Frontier

https://doi.org/10.1021/acsomega.3c06271
ACS Omega 2023, 8, 38748−38765

Orbital Energy Levels of Conjugated Polymers for Solar Cell Applications. *Adv. Mater.* **2011**, *23* (20), 2367−2371.
(124) Meng, S.; Ren, J.; Kaxiras, E. Natural Dyes Adsorbed on TiO_2 Nanowire for Photovoltaic Applications: Enhanced Light Absorption and Ultrafast Electron Injection. *Nano Lett.* **2008**, *8* (10), 3266−3272.
(125) Maurya, I. C.; Neetu; Gupta, A. K.; Srivastava, P.; Bahadur, L. Callindra Haematocephata and Peltophorum Pterocarpum Flowers as Natural Sensitizers for TiO_2 Thin Film Based Dye-Sensitized Solar Cells. *Opt. Mater.* **2016**, *60*, 270−276.
(126) Nemade, A. M.; Patil, K. D.; Kolhe, V. C. Synthesis, Compositional and Spectral Studies of Some Transition Metal Complexes with 3-Aminolawsonoxime. *Res. J. Chem. Sci.* **2017**, *7* (1), 25−31.
(127) Sahoo, S. S.; Salunke-Gawali, S.; Jagtap, C. V.; Bhujbal, P.; Pathan, H. M. Enhanced Photovoltage Production from Canna Dyes with Surface Passivation of ZnO Based Dye Sensitized Solar Cells. *Journal of Science: Advanced Materials and Devices* **2022**, *7* (4), 100513.
(128) Lenzmann, F.; Krueger, J.; Burnside, S.; Brooks, K.; Grätzel, M.; Gal, D.; Rühle, S.; Cahen, D. Surface Photovoltage Spectroscopy of Dye-Sensitized Solar Cells with TiO_2, Nb_2O_5, and $SrTiO_3$ Nanocrystalline Photoanodes: Indication for Electron Injection from Higher Excited Dye States. *J. Phys. Chem. B* **2001**, *105* (27), 6347−6352.
(129) Waghmare, M. A.; Naushad, Mu.; Pathan, H. M.; Ubale, A. U. Rose Bengal-Sensitized ZrO_2 Photoanode for Dye-Sensitized Solar Cell. *J. Solid State Electrochem* **2017**, *21* (9), 2719−2723.
(130) Bramhankar, T. S.; Pawar, S. S.; Shaikh, J. S.; Gunge, V. C.; Beedri, N. I.; Baviskar, P. K.; Pathan, H. M.; Patil, P. S.; Kambale, R. C.; Pawar, R. S. Effect of Nickel-Zinc Co-Doped TiO_2 Blocking Layer on Performance of DSSCs. *J. Alloys Compd.* **2020**, *817*, 152810.
(131) Shaikh, J. S.; Shaikh, N. S.; Mali, S. S.; Patil, J. V.; Pawar, K. K.; Kanjanaboos, P.; Hong, C. K.; Kim, J. H.; Patil, P. S. Nanoarchitectures in Dye-Sensitized Solar Cells: Metal Oxides, Oxide Perovskites, and Carbon-Based Materials. *Nanoscale* **2018**, *10* (11), 4987−5034.
(132) Yeoh, M.-E.; Chan, K.-Y. Recent Advances in Photo-Anode for Dye-Sensitized Solar Cells: A Review: Recent Advances in Photo-Anode for DSSCs: A Review. *Int. J. Energy Res.* **2017**, *41* (15), 2446−2467.
(133) Yang, W.-G.; Wan, F.-R.; Chen, Q.-W.; Li, J.-J.; Xu, D.-S. Controlling Synthesis of Well-Crystallized Mesoporous TiO_2Microspheres with Ultrahigh Surface Area for High-Performance Dye-Sensitized Solar Cells. *J. Mater. Chem.* **2010**, *20* (14), 2870.
(134) Lee, K.; Hu, C.; Chen, H.; Ho, K. Incorporating Carbon Nanotube in a Low-Temperature Fabrication Process for Dye-Sensitized TiO_2 Solar Cells. *Sol. Energy Mater. Sol. Cells* **2008**, *92* (12), 1628−1633.
(135) Du, P.; Song, L.; Xiong, J.; Yuan, Y.; Wang, L.; Xi, Z.; Jin, D.; Chen, J. TiO_2/Nb_2O_5 Core-Sheath Nanofibers Film: Co-Electrospinning Fabrication and Its Application in Dye-Sensitized Solar Cells. *Electrochem. Commun.* **2012**, *25*, 46−49.

https://doi.org/10.1021/acsomega.3c06271
ACS Omega 2023, 8, 38748−38765